

Spectroscopic Characterization, Cyclic Voltammetry, Biological Investigations, MOE, and Gaussian Calculations of VO(II), Cu(II), and Cd(II) Heteroleptic Complexes

Anwer G. Al-Harazie,* Esam A. Gomaa, Rania R. Zaky, and Mahmoud N. Abd El-Hady



Cite This: *ACS Omega* 2023, 8, 13605–13625



Read Online

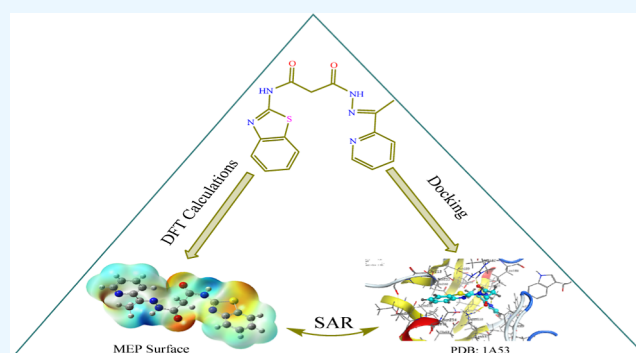
ACCESS |

Metrics & More

Article Recommendations

Supporting Information

ABSTRACT: A novel hydrazone ligand (*o*-H₂BMP) *N*-(benzo[*d*]thiazol-2-yl)-3-oxo-3-(2-(1-(pyridin-2-yl)ethylidene)hydrazinyl)propanamide alongside its Cu(II), Cd(II), and VO(II) complexes were prepared and structurally characterized via various spectroscopic analyses (Fourier transform infrared spectroscopy, UV–visible spectroscopy, ¹H/¹³C NMR spectroscopy, liquid chromatography coupled to mass spectrometry, and electron paramagnetic resonance spectroscopy) as well as by elemental analysis, thermal gravimetry analysis/differential thermal analysis, and magnetic moment measurements. Powder X-ray diffraction analysis was also performed for the free ligand and its metal complexes to determine the crystallographic structures and atomic spacing. It also provided information on unit cell dimensions and the average crystallite size. Furthermore, geometric optimization and computational studies were carried out by applying Gaussian (09) software based on density-functional theory coupled with the B3LYP functional and LANL2DZ/6-31+G(d,p) mixed basis set to evaluate some distinct features such as molecular electrostatic potential, E_{HOMO} , and E_{LUMO} . Moreover, electrochemical measurements were performed for Cu(II) in the absence/presence of the chelating agent to predict the effect of complexation interaction in the solution state study. As part of the biological examination, antioxidant and antimicrobial assays were conducted for each compound individually, in addition to cytotoxicity evaluations via MTT assays for all isolated complexes compared to the corresponding metal salts. The MOE (molecular operating environment) approach was also applied to model the interface between the isolated compounds and proteins that were expressed in breast cancer at the atomic level.



1. INTRODUCTION

Hydrazones belong to the Schiff base family and have played an imperative role in the development of coordination chemistry owing to their chelating properties.^{1–3} Generally, hydrazones are characterized by an imine group, providing information about the mechanism as well as the interaction in the biochemical system, where these compounds have a significant impact in pharmaceutical fields due to their wide bioactive efficacy.⁴ As a result of these significant biological applications of metal complexes, they have received a great deal of attention and are considered models of biologically relevant organisms. An extensive range of biological activities were demonstrated for these compounds, including anti-diabetic, antifungal, antibacterial, anticancer, antitumor, and antiproliferative activities.⁵

In particular, 2-acetylpyridine hydrazone derivatives of benzothiazole exhibit a potent toxic effect on lymphomas, leukemias, and breast tumors.^{6,7} Also, Cu(II) complexes are more potent against rheumatoid arthritis and ulcers due to their role as acidic anti-inflammatory supplementary agents in gastrointestinal damage.⁸ Moreover, VO(II) complexes

showed a very similar strength of activity to standard drugs such as ciprofloxacin (an antibacterial drug) and clotrimazole (an antifungal drug).⁹ Further, Cd(II) complexes with some hydrazone derivatives, such as ethyl-2-[(pyridine-2-ylmethylene)hydrazino] acetate, showed very similar biological activity to ampicillin as an antibacterial drug.¹⁰

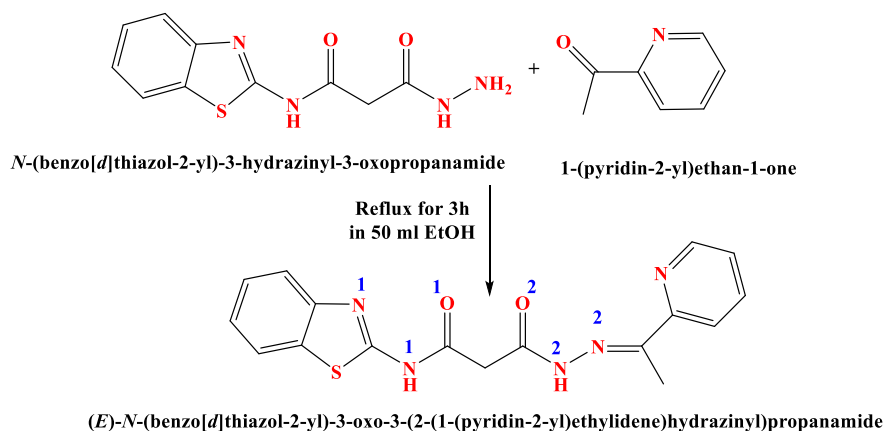
In the present study, we aim to synthesize transition-metal complexes of VO(II), Cu(II), and Cd(II) cations using a novel *N*-(benzothiazol-2-yl)-3-oxo-3-(2-(1-(pyridin-2-yl)ethylidene)hydrazinyl)propanamide in conjunction with experimental and theoretical characterizations. In addition to providing qualitative information about the redox process and thermodynamic parameters, cyclic voltammetry (CV) was also employed to analyze the Cu(II) species. Finally, a biological investigation

Received: November 28, 2022

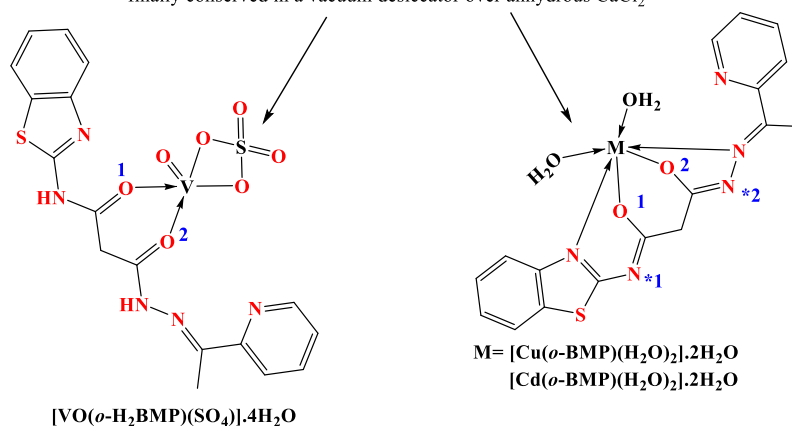
Accepted: March 28, 2023

Published: April 4, 2023



Scheme 1. Synthesis of *o*-H₂BMP Ligand and Its Metal Complexes

The Cu(II), Cd(II) and VO(II) complexes were formed by mixing equimolar amounts of the (*o*-H₂BMP) ligand (0.53 gm) with absolute ethanolic and/or aqueous solution salts of CuCl₂·2H₂O (0.256 gm), CdCl₂·H₂O (0.302 gm), and VO(SO₄)·5H₂O (0.38 gm). The reaction mixture was heated under reflux (1-3) hours. The precipitate was filtered off, washed with hot EtOH and/or H₂O, and finally conserved in a vacuum desiccator over anhydrous CaCl₂.



was conducted, which included tests for antimicrobial, antioxidant, and MTT activity. Molecular docking allowed us to predict the behavior of investigated compounds toward the binding sites of target proteins as well as to investigate fundamental biochemical processes.

2. MATERIALS AND METHODS

2.1. Chemicals. The chemicals CuCl₂·2H₂O, CdCl₂·H₂O, VO(SO₄)·5H₂O, DMSO, KCl, 3-(benzo[*d*]thiazol-2-ylamino)-3-oxopropanoyl chloride, hydrazine hydrate, 2-acetyl pyridine, glacial acetic acid, and absolute EtOH were used without any treatment and were provided by BDH, Sigma-Aldrich, and Merck companies.

2.2. Synthesis of Ligand *o*-H₂BMP and Complexes. The synthesis of *N*-(benzothiazol-2-yl)-3-oxo-3-(2-(1-(pyridin-2-yl)ethylidene)hydrazinyl)-propanamide ligand (*o*-H₂BMP) was accomplished by heating under reflux a mixture of *N*-(benzo[*d*]thiazol-2-yl)-3-hydrazinyl-3-oxopropanamide (0.01 m; 2.503 gm) with 1-(pyridin-2-yl)ethan-1-one (0.01 m; 1.21 gm) on addition drops of glacial acetic acid for 3 h.^{11,12} After completion of the reaction, a newly formed product of yellowish-white precipitate was obtained, which was confirmed by thin layer chromatography (TLC) and separated by filtration, followed by washing with absolute EtOH. In addition, Cu(II), Cd(II), and VO(II) complexes were formed according to Scheme 1.

2.3. Analysis of *o*-H₂BMP Ligand and Its Complexes.

The percentages of C, H, and N for the (*o*-H₂BMP) ligand and its metal complexes were performed in Microanalytical Unit, Ain Shams University, Egypt. Also, the metal cations' contents were determined by complexometric titrations. The content of sulfate in the VO(II) complex was detected by gravimetric analysis in the form of barium sulfate. The instruments used to elucidate the structures of the isolated compounds were Fourier-transform infrared (FT-IR) spectroscopy, UV–visible spectroscopy, ¹H/¹³C NMR spectroscopy, LC coupled to mass spectrometry (LC–MS), electron spin resonance (ESR) spectroscopy, powder X-ray diffraction (PXRD) analysis, thermogravimetric analysis/differential thermal analysis (TGA/DTA), and magnetic susceptibility balance measurements. CV was performed by a DY 2100 potentiostat with three electrodes (glassy carbon as a working electrode, platinum as an auxiliary electrode, and Ag/AgCl as a reference electrode) that were immersed in a cell containing 0.1 M of KCl solution as a supporting electrolyte^{13,14} as shown in Scheme 1S.

2.4. Gaussian Calculations. The density-functional theory (DFT) calculations were performed using Gaussian 09 software on applying the B3LYB functional and the LANL2DZ/6-31+G(d,p) mixed basis set to realize the geometric optimized structures of the isolated solid compounds except for the ligand, which is obtained by using the 6-31+G(d,p) basis set.^{15–18}

Table 1. Physical Properties and Elemental Analysis of *o*-H₂BMP Ligand and Its Complexes

no.	compound (chemical formula)	m. wt	(a) physical properties		(b) elemental analysis: found (calcd)					
			mp	color	% C	% N	% H	% S	% M	SO ₄
1	<i>o</i> -H ₂ BMP (C ₁₇ H ₁₅ N ₅ O ₂ S)	353.40	214	yellowish white	57.33 (57.78)	19.83 (19.82)	4.29 (4.28)	8.76 (9.07)	–	–
2	[VO(<i>o</i> -H ₂ BMP)(SO ₄)]·4H ₂ O (C ₁₇ H ₂₃ N ₅ O ₁₁ S ₂ V)	588.46	>300	olive	35.20 (34.70)	11.69 (11.90)	4.31 (3.94)	11.04 (10.90)	8.45 (8.66)	15.8 (16.31)
3	[Cu(<i>o</i> -BMP)(H ₂ O) ₂]·2H ₂ O (C ₁₇ H ₂₁ N ₅ O ₆ SCu)	486.99	>300	brown	42.61 (41.93)	14.85 (14.38)	4.09 (4.35)	6.05 (6.58)	11.31 (13.05)	–
4	[Cd(<i>o</i> -BMP)(H ₂ O) ₂]·2H ₂ O (C ₁₇ H ₂₁ N ₅ O ₆ SCd)	535.86	>300	yellow	38.78 (38.10)	13.65 (13.07)	4.22 (3.95)	6.21 (5.98)	20.83 (20.98)	–

Table 2. Most Characteristic FT-IR Bands of Ligand 1 (*o*-H₂BMP) and Its Complexes

	$\nu(\text{C}=\text{O})_{\text{thiazole}}^1$	$\nu(\text{C}=\text{O})_{\text{azo}}^2$	$\nu(\text{C}=\text{N})_{\text{thiazole}}^1$	$\nu(\text{C}=\text{N})_{\text{azo}}^2$	$\nu(\text{NH})_{\text{thiazole}}^1$	$\nu(\text{NH})_{\text{azo}}^2$	$\nu(\text{C}=\text{N})_{\text{thiazole}}^{*1}$	$\nu(\text{C}=\text{N})_{\text{azo}}^{*2}$	$\nu(\text{C}=\text{O})_{\text{thiazole}}^1$	$\nu(\text{C}=\text{O})_{\text{azo}}^2$
1	1652	1696	1628	1605	3216	3180	–	–	–	–
2	1646	1678	1627	1604	3223	3178	–	–	–	–
3	–	–	1605	1582	–	–	1634	1629	1271	1103
4	–	–	1600	1589	–	–	1638	1630	1268	1108

2.5. Antioxidant Activity (DPPH, ABTS). The DPPH (1,1-diphenyl-2-picrylhydrazyl) and ABTS [2,2-azinobis-(3-ethylbenzothiazoline-6-sulfonic acid)] assays are widely used in antioxidant studies because these methods are simple and very sensitive colorimetric techniques that rely on the production of colorful mono-cationic free radicals within a strong absorption (deep purple at λ 517 nm for DPPH⁺ and green-blue at λ 734 nm for ABTS⁺). A significant decrease in the measured absorbance of these radicals, which act as hydrogen acceptors, is observed when hydrogen donor antioxidants are present. Thus, the inhibition percentage can be calculated using L-ascorbic acid as a reference standard antioxidant,^{19–21} as shown in Scheme 2S.

2.6. Microbial Study. The antimicrobial activity was done by disc diffusion technique^{21,22} as shown in Scheme 3S. The microbial strains tested are *Staphylococcus aureus*, *Bacillus subtilis*, *Escherichia coli*, *Salmonella typhi*, and *Candida albicans*. The percentage of antimicrobial activity and anti-fungal activity for the compounds was evaluated by comparison with gentamycin and clotrimazole standards.²³

2.7. MTT Assay. The antitumor efficiency of the free ligand and its metal complexes were examined in vitro against breast cancer cells (MDA-MB-231 and MCF-7). The examined compounds were dissolved in DMSO by 10 mM stock and stored at –20 °C, and cisplatin was used as a positive control. Cells were cultured using Dulbecco's modified Eagle's medium in a 96-walled plate and completed with 10% fetal bovine serum with (100 IU/mL) penicillin/streptomycin (100 μ g/mL) (Lonza, 17-602E) at 95% air condition with 5% of CO₂ in 37 °C. The initial screening and cell viability were assessed by MTT assay,^{24–28} in which the absorbance was measured at λ 570 nm by a Biotek plate reader (Gen5), as shown in Scheme 4S.

2.8. Molecular Docking. MOE (molecular operating environment 2015) software was used to carry out molecular docking calculations of the prepared compounds with protein receptors 6CBZ, 1FDW, 2WTT, 4GL7, 1A53, and 1X7R, which are expressed more during breast cancer. All proteins were obtained as PDB files from the Protein Data Bank. Water molecules connected to these proteins were excluded to avoid interfering with the docking study. The structures were drawn by using ChemDraw 15 software. These compounds were then

docked into the active sites of selected proteins individually.^{29,30}

3. RESULTS AND DISCUSSION

3.1. Elemental Analyses and Physical Properties. The elemental analysis results with some physical properties are presented in Table 1 in which the calculated and experimental percentages strongly coincided with each other, confirming the proposed chemical formula. The *o*-H₂BMP ligand reacted with the VO(II), Cu(II), and Cd(II) ions to form five- or six-membered ring chelates. According to the outcomes data, the isolated solid complexes have a stoichiometric ratio of 1 M/1 L). The measured molar conductance value for VO(II) complex (10^{–3} M) at room temperature in DMSO is 18 μ S cm² mol^{–1}. Therefore, it is concluded that the SO₄^{2–} ion is bonded to the VO(II) ion, indicating its coordinating nature.

3.2. FT-IR Spectra. The FT-IR spectrum of the hydrazone ligand (*o*-H₂BMP) revealed various important characteristic bands at 1652, 1696, 1628, 1605, 3216, 3180, and 689 cm^{–1} that belong to $\nu(\text{C}=\text{O})^1$, $\nu(\text{C}=\text{O})^2$, $\nu(\text{C}=\text{N})^1$ and $\nu(\text{C}=\text{N})^2$, $\nu(\text{NH})^1$, $\nu(\text{NH})^2$ and breathing mode of vibration for pyridine ring $\nu(\text{C}=\text{N})_{\text{pyr}}$ correspondingly.

The spectrum of the [VO(*o*-H₂BMP)(SO₄)]·4H₂O complex showed that the (*o*-H₂BMP) coordinated as a neutral bidentate ligand via $\nu(\text{C}=\text{O})^1$ and $\nu(\text{C}=\text{O})^2$ groups according to the following variations: (i) the change in the intensity of the two carbonyl bands (C=O)¹ and (C=O)² as well as the shift of these two groups to lower wavenumbers of 1646 and 1678 cm^{–1}, respectively; (ii) the appearance of a new $\nu(\text{SO}_4^{2-})$ at 1041 and 1164 cm^{–1}, predicting the bidentate nature;^{31,32} and (iii) the presence of new $\nu(\text{V}=\text{O})$ at 980 cm^{–1},^{33,34} and $\nu(\text{V}-\text{O})$ at 513 cm^{–1}.

While the IR spectrum of both [Cu(*o*-BMP)(H₂O)₂]·2H₂O and [Cd(*o*-BMP)(H₂O)₂]·2H₂O complexes deduced the binate tetradentate chelation via two enolic oxygens (=C–O)¹, (=C–O)², and two azomethine nitrogens (C=N)¹, (C=N)² based on the following observations: (i) disappearance of $\nu(\text{C}=\text{O})^1$, $\nu(\text{C}=\text{O})^2$, $\nu(\text{NH})^1$ and $\nu(\text{NH})^2$ with a simultaneous appearance of new enolic $\nu(\text{C}-\text{O})^1$, $\nu(\text{C}-\text{O})^{235}$ and azomethine $\nu(\text{C}=\text{N})^{*1}$, $\nu(\text{C}=\text{N})^{*2}$ groups at (1271, 1268) cm^{–1}, (1103, 1108) cm^{–1}, (1634, 1638) cm^{–1}, and (1629, 1630) cm^{–1}, correspondingly; (ii) shift of $\nu(\text{C}=\text{N})^1$, $\nu(\text{C}=\text{N})^2$ to lower wavenumber at (1605, 1600) cm^{–1} and

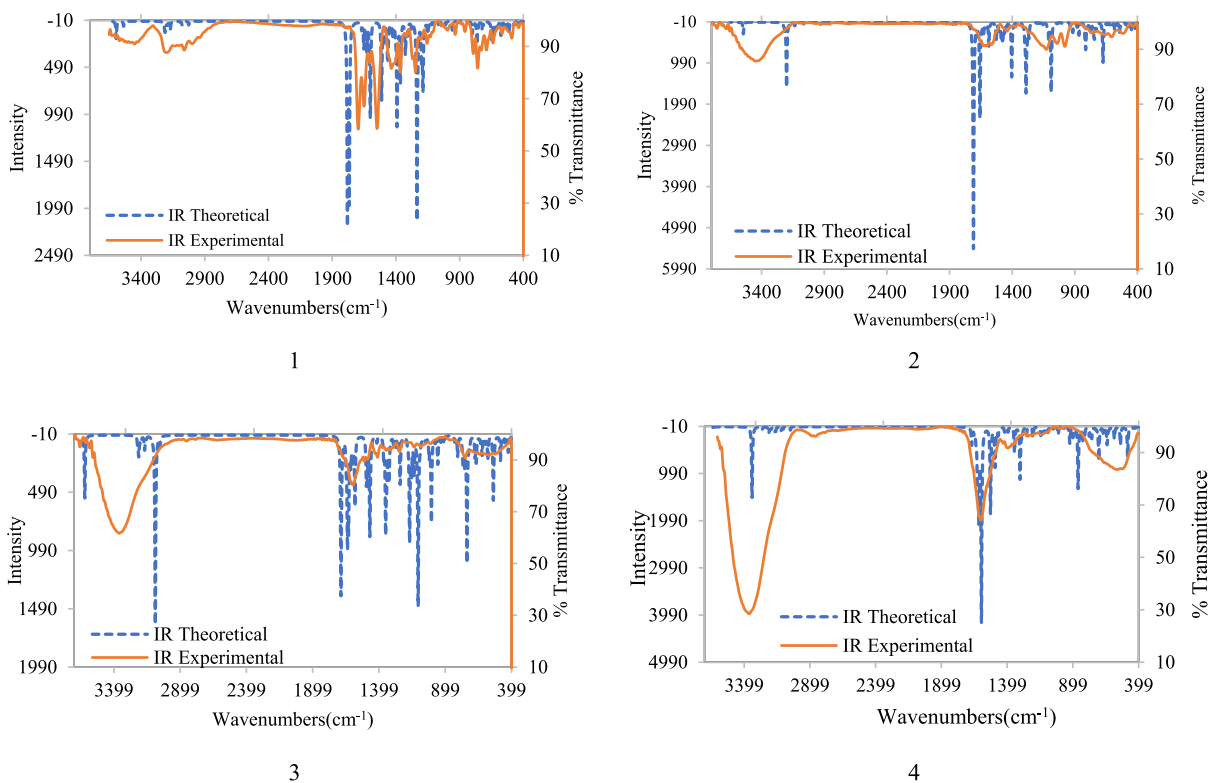


Figure 1. Experimental and theoretical IR spectra of (1) *o*-H₂BMP, (2) [VO(*o*-H₂BMP)(SO₄)]·4H₂O, (3) [Cu(*o*-BMP)(H₂O)₂]·2H₂O, and (4) [Cd(*o*-BMP)(H₂O)₂]·2H₂O.

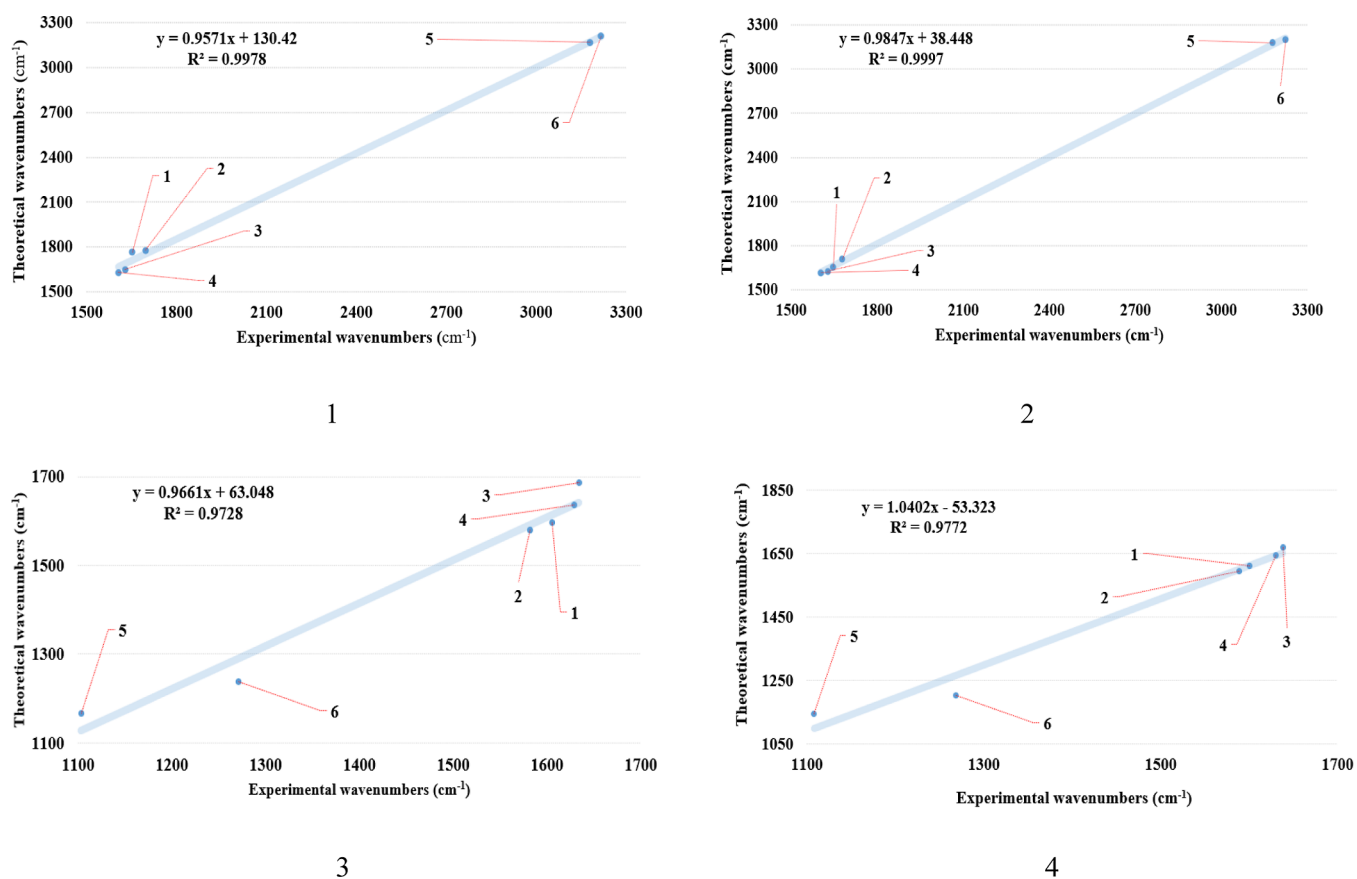


Figure 2. Correlation plots of experimental and theoretical data for the most characteristic IR bands of (1) *o*-H₂BMP, (2) [VO(*o*-H₂BMP)(SO₄)]·4H₂O, (3) [Cu(*o*-BMP)(H₂O)₂]·2H₂O, and (4) [Cd(*o*-BMP)(H₂O)₂]·2H₂O.

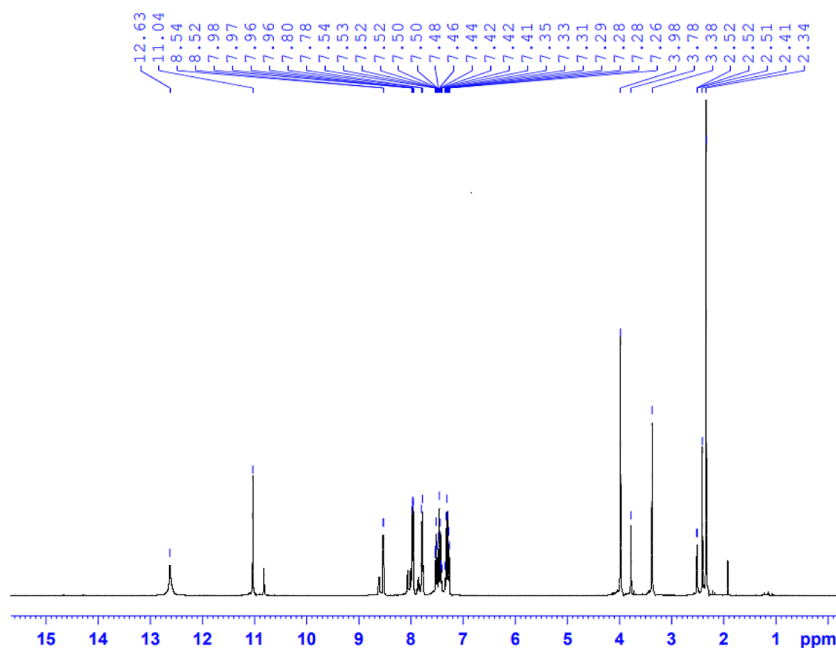


Figure 3. ^1H NMR spectrum of *o*-H₂BMP.

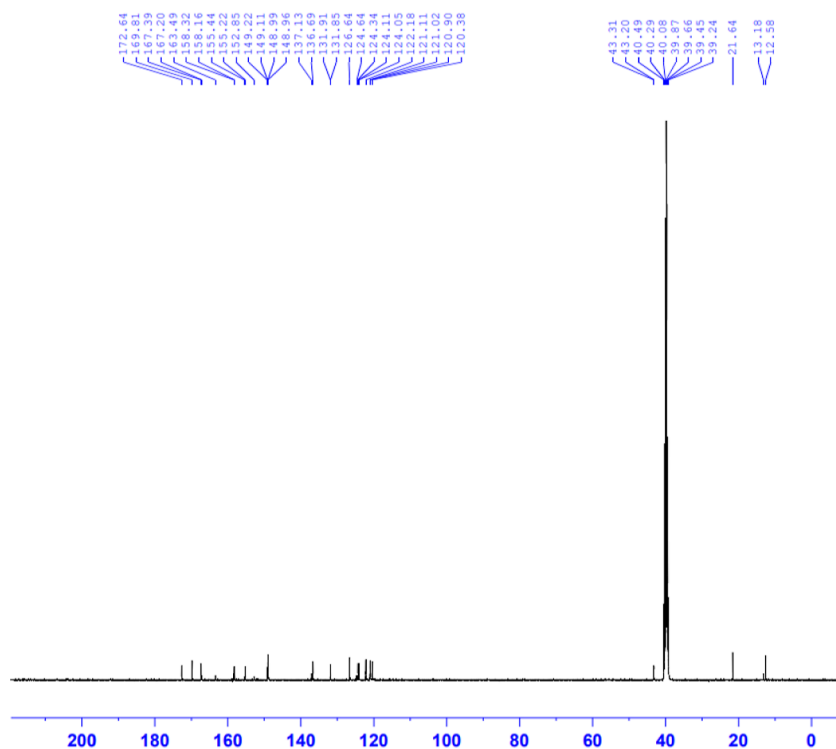


Figure 4. ^{13}C NMR spectrum of *o*-H₂BMP.

(1582, 1589) cm^{-1} , respectively; and (iii) existence of new bands for $\nu(\text{M}-\text{O})$ at (575, 570) cm^{-1} and $\nu(\text{M}-\text{N})$ at (446, 443) cm^{-1} , correspondingly. All the most characteristic FT-IR bands of the ligand and its complexes are listed in the Table 2.

3.2.1. Correlation Analysis. Correlation analysis has been established between the experimental and theoretical absorption bands deduced from the infrared spectroscopic investigations, where the theoretical absorption bands were computed from DFT frequency data and the experimental absorption bands were detected from the measured IR spectra

of solid compounds. The converge diagrams in conjugation with the scatter plots were used to clarify the statistical correlation.³⁶ Based on the results in Figures 1 and 2 and Table 1S, it was evident that all compounds had a strong positive linear correlation, with R^2 ranging between 0.9728 and 0.9997.

3.3. ^1H NMR and ^{13}C NMR. The ^1H NMR spectrum of *o*-H₂BMP as illustrated in Figure 3 showed amide-iminol tautomerism (Scheme 5S) according to the following observations: (i) imide proton (NH)¹ appeared at chemical shift (δ) 12.63 ppm for both tautomers; (ii) imide proton

(NH)² for iminol tautomer appeared at (δ) 10.85 ppm; (iii) enolic proton (O–H) appeared at (δ) 11.04 ppm which predicted the enolization of (*o*-H₂BMP) ligand; (iv) aromatic protons existed in the range of (δ) 7.26–8.54 ppm in both tautomeric structures; (v) two singlet signals for methylene and methyl protons (CH₂), (CH₃) at (δ) 3.98, δ 2.43 ppm for amide moiety, and (δ) 3.78, 2.52 ppm for iminol moiety, respectively.

The ¹³C NMR spectrum of *o*-H₂BMP as demonstrated in Figure 4 showed the following remarks: (i) aromatic carbons appeared in the range of δ 121.00–132.65 ppm in both tautomeric structures; (ii) cyclic carbons existed in the range of δ 21.73–29.26 ppm for both two tautomeric structures; (iii) in amide tautomer, sharp peaks at (δ) 167.46, 165.58, 158.39, 140.26, and 43.37 ppm are assigned to (C=N)¹, (C=O)², (C=O)¹, (C=N)², and (CH₂), respectively; and (iv) in imidic acid form, sharp peaks at δ 169.65, 167.20, 158.11, 149.07, and 42.24 ppm which correspond to (C=N)¹, (C=N)^{*}, (C=O)¹, (C=N)², and (CH₂), respectively.

In a comparison of the ¹H NMR spectrum of the free ligand with [Cd(*o*-BMP)(H₂O)₂].2H₂O as in Figure 1S, it was noticed that the absence of any protons possessed imide or enolic groups for both tautomers, which predicted the hydrazone reacted as a bi-negative ligand via two enolic groups as a result of the enolization of two carbonyls. It also showed sharp two-singlet peaks at δ 3.3–3.5 ppm for methylene group protons, δ 2.5–2.52 ppm for methyl protons, and multiple δ 7.24–8.62 ppm for aromatic benzene and pyridine ring protons.

3.4. UV–Visible and Magnetism. The qualitative UV–visible spectra were obtained in the DMSO solvent to obtain smooth absorption curves as shown in Figure 2S. Interligand transition bands appearing at 35,971, 33,898, and 27,778 cm⁻¹ are attributed to $n \rightarrow \sigma^*$, $\pi \rightarrow \pi^*$, and $n \rightarrow \pi^*$ transitions, respectively. A structurally condensed conjugation of chromophores leads to the appearance of a yellowish-white color for the hydrazone ligand. The VO(II) complex displayed a band at 19,685 cm⁻¹ assigned to ²B₂ → ²E₂(ν_2). This spectrum, accompanied by the magnetic moment value ($\mu_{\text{eff}} = 1.79$ BM), is attributed to the square pyramidal configuration.^{37–39} Whereas, the electronic spectrum of the Cu(II) complex displayed two transition bands at 16,207 and 14,771 cm⁻¹ assigned to ²B_{1g} → ²E_g and ²B_{1g} → ²A_{1g} transitions, respectively, which indicated the existence of a distorted octahedral geometry around the Cu(II) ion.⁴⁰ Also, the magnetic moment value of [Cu(*o*-BMP)(H₂O)₂].2H₂O is 2.13 BM.

3.5. EPR Studies. EPR spectra of VO(II) and Cu(II) complexes (Figure 5) were recorded using a Bruker EMX spectrometer operating at room temperature in the X-band (9.685 GHz) with a 100 kHz modulation frequency.

The EPR spectrum of the Cu(II) complex displayed a four-line hyperfine pattern with spin Hamiltonian parameters ($I = 3/2$, $S = 1/2$) that showed axial symmetry similarity for g-tensor parameters (g_{\parallel} , 2.26 > g_{\perp} , 2.09 > g_e , 2.0023), indicating that Cu(II) has a $d_{x^2-y^2}$ ground-state with octahedral geometry.⁴¹ These g-tensor parameters were calculated from the EPR spectrum by applying eq 1^{42–44}

$$g = h\nu/\mu B \quad (1)$$

where h is the Planck constant (6.626×10^{-34} J), ν is the frequency (9.865 MHz), μ the is applied magnetic field in mT, and B is the Bohr magneton (9.27×10^{-24} J/mT).

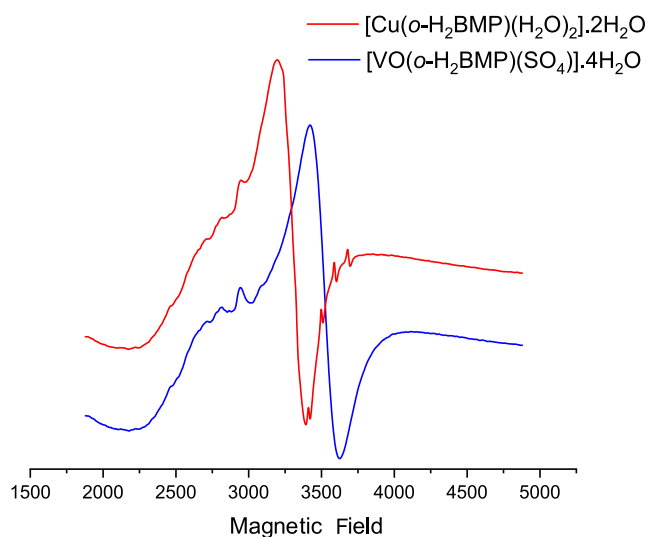


Figure 5. EPR spectra of [Cu(*o*-BMP)(H₂O)₂].2H₂O and [VO(*o*-H₂BMP)(SO₄)].4H₂O complexes.

Consequently, the G -factor for axial symmetry could be calculated from eq 2

$$G = (g_{\parallel} - 2)/(g_{\perp} - 2) = 4 \quad (2)$$

Essentially, G is a measure of the exchange interaction between Cu(II) centers in the solid state complex, which is negligible if G is greater than 4, while if G is less than 4, there is a considerable exchange interaction in the Cu(II) complex.⁴⁵ In addition, the parallel and perpendicular hyperfine parameters (A_{\parallel} , 0.0152 and A_{\perp} , 0.0531) components were estimated from the spectrum. Furthermore, the F -factor was determined by applying eq 3

$$F = g_{\parallel}/A_{\perp} \quad (3)$$

Basically, the F -factor is used to quantify the degree of distortion of the Cu(II) complex. Where, if the F -factor value is between (105 and 135), the complex is square-planar, while the tetrahedrally distorted structure can have a much larger value (>135). The F -factor value for the Cu(II) complex was achieved (148.38), predicting the existence of distorted octahedral geometry.

The molecular orbital coefficients, covalent in-plane σ -bonding (α^2), and covalent in-plane π -bonding (β^2) were calculated using eqs 4 and 5

$$\alpha^2 = (A_{\parallel}/0.036) + (g_{\parallel} - 2.0023) + 3/7(g_{\perp} - 2.0023) + 0.04 \quad (4)$$

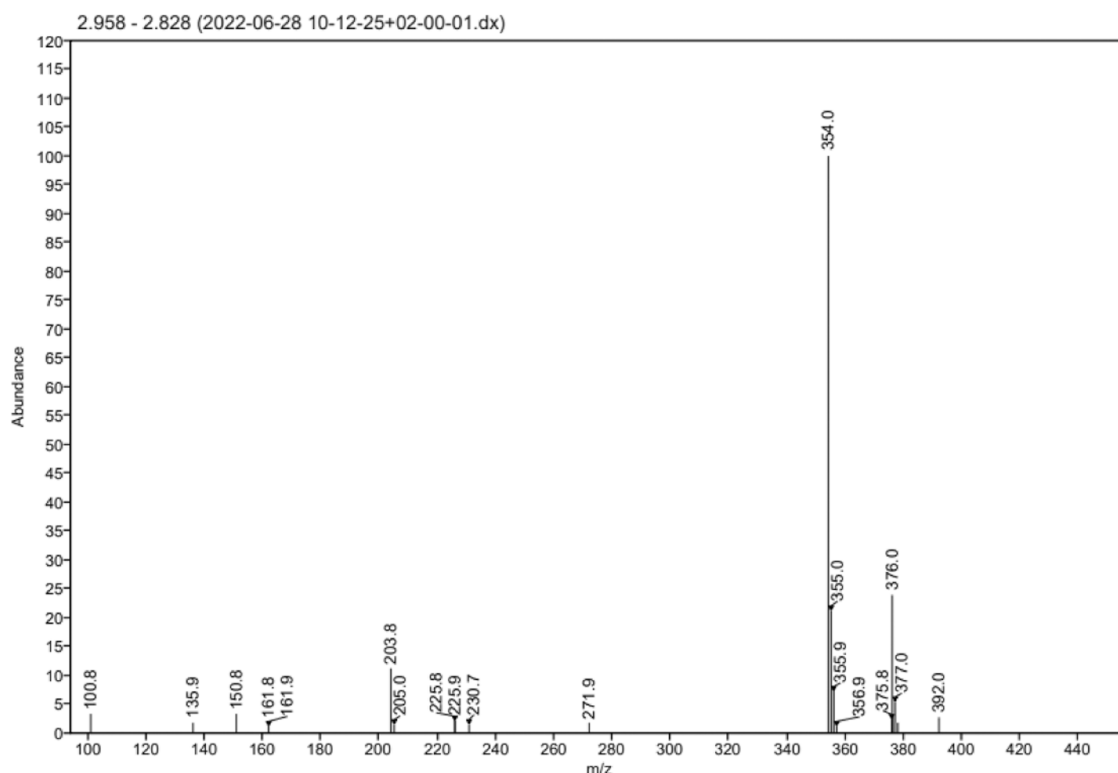
$$\beta^2 = (g_{\parallel} - 2.0023)E - 8\lambda\alpha^2 \quad (5)$$

where E is the energy of electronic transition on the UV spectrum, and $\lambda = -828$ cm⁻¹ for the free Cu(II) ion. The factor ($\alpha^2 = 1$) represents a full ionic character, whereas ($\alpha^2 = 0.5$) represents absolute covalent bonding, and the small values are negligible. As the β^2 value decreases, the covalent in-plane π -bonding covalence increases.⁴⁶ The Cu(II) complex has very strong in-plane π -bonding, based on the values of $\alpha^2 = 0.75$ and $\beta^2 = 0.75$. These results are expected due to the ligand having orbitals that combine with the d_{xy} orbital in the copper ion.

Table 3. ESR Parameters for Cu(II) and VO(II) Complexes

no.	g_{\parallel}	g_{\perp}	A_{\parallel} (cm ⁻¹)	A_{\perp} (cm ⁻¹)	G	F	α^2	β^2
2	1.93	1.95	0.0173	0.0086	1.5	111.78	0.23	2.45
3	2.26	2.09	0.0152	0.0531	2.9	148.38	0.75	0.75

Signal Name MS1 +TIC SCAN ESI Frag=110V Gain=1.0
 Peak Retention Time 2.958

Figure 6. Mass spectrum of *o*-H₂BMP.

The EPR spectrum of the VO(II) complex gave a typical eight-line characteristic pattern of interaction with spin Hamiltonian parameters ($S = 1/2$ and $I = 7/2$) and one unpaired electron ($3d^1$) in the VO(II) ion. The EPR parameters (g_{\parallel} , g_{\perp} , A_{\parallel} , A_{\perp} , G , F) calculated for the [VO(*o*-H₂BMP)(SO₄)]·4H₂O complex are presented in Table 3, while the molecular orbital α^2 and β^2 coefficients were applied using eqs 6 and 7⁴⁷

$$\alpha^2 = E(g_e - g_{\parallel})/8\beta^2\lambda \quad (6)$$

$$A_{\parallel} = -P\kappa + (4/7)\beta^2P - (g_e - g_{\parallel})P - (3/7)(g_e - g_{\perp})P \quad (7)$$

where λ for VO(II) ion = 170 cm⁻¹, and the Fermi contact (κ), a measure of the d-orbital population for unpaired electron, was calculated from eqs 8 and 10

$$\kappa = A_{\text{iso}}/P(g_e - g_{\text{iso}}) \quad (8)$$

$$g_{\text{iso}}(2g_{\perp} + g_{\parallel})/3 \quad (9)$$

$$A_{\text{iso}}(2A_{\perp} + A_{\parallel})/3 \quad (10)$$

where P is the constant of direct dipole–dipole interaction between the electron and the magnetic moment of the

vanadium nucleus (0.0136 cm⁻¹).⁴⁸ The VO(II) complex gave ($G = 1.5 < 4$), which indicated the exchange interaction between VO(II) centers in the solid state, and the F -factor was 111.78, which is less than 135 indicating the square-pyramidal geometry around the VO(II) ion.

The calculated ($\beta^2 = 2.45$) value which deviated from the expected range between (0.93–1) indicated the increase of the covalency degree, and this is a measure for the bonding between the d_{xy} orbital of VO(II) with the π -orbitals of the ligand. As a result, the α^2 value ($\alpha^2 = 0.23$) showed a very strong in-plane π -bonding.^{49,50} This more covalent bonding resulted in the appearance of an overlapped hyperfine splitting within small variations between the g -values (g_{\parallel} , 1.93 < g_{\perp} , 1.95 < g_e , 2.0023) and A -values (A_{\parallel} , 0.0173 and A_{\perp} , 0.0086).

3.6. LC–MS. The mass spectrum of the *o*-H₂BMP ligand was obtained^{51–53} by using the LC/MSD iQ instrument at a retention time of 2.958 min, as shown in Figure 6. The molecular ion peak [m/z] of the free ligand was observed at 354, which approximately corresponds to the exact molecular weight.

3.7. TGA/DTA. Thermal analysis was measured for the isolated complexes to determine the water molecules' nature, as coordinated or crystalline Table 3S. TGA curves are

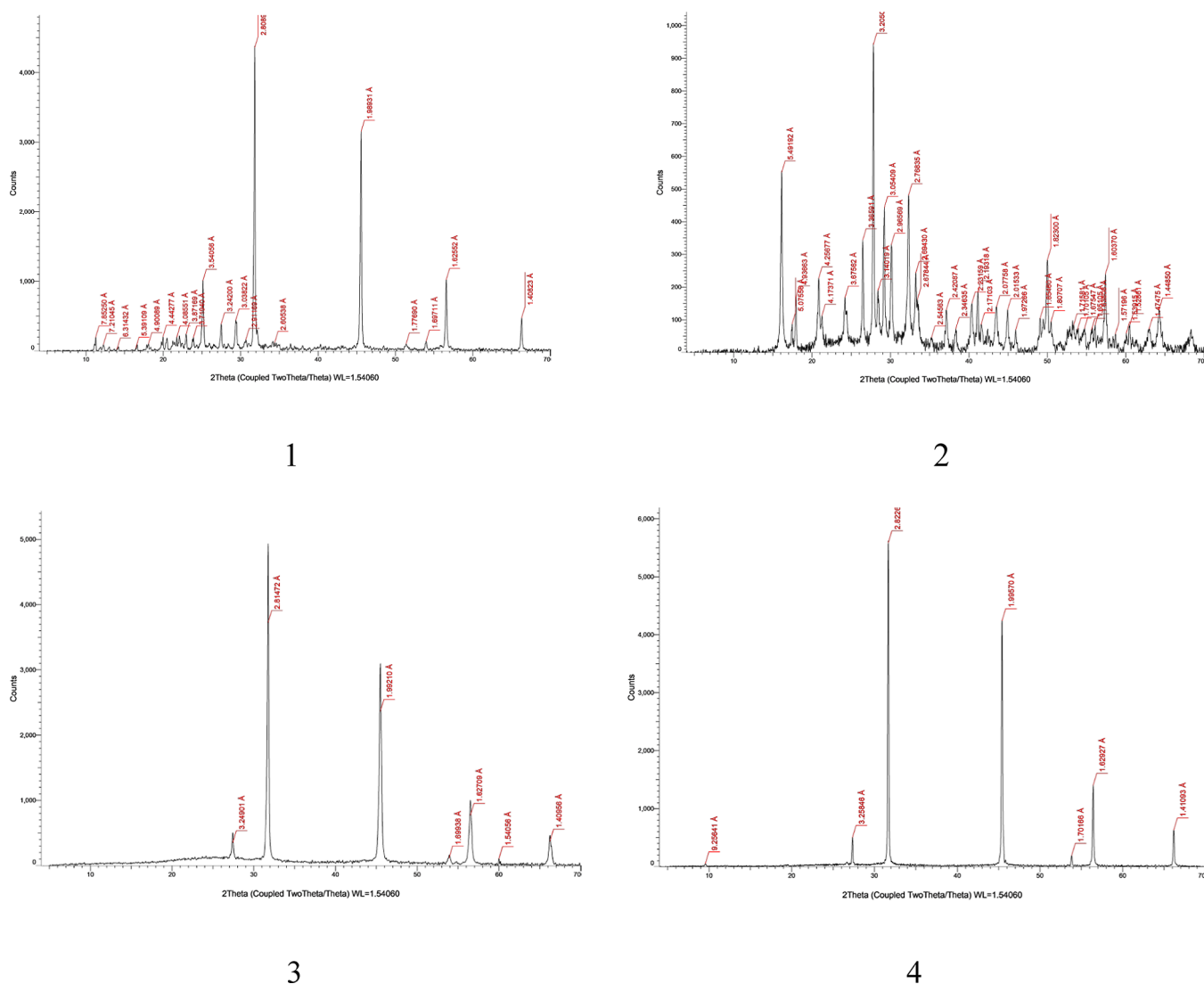


Figure 7. PXRD patterns of (1) *o*-H₂BMP, (2) [VO(*o*-H₂BMP)(SO₄)]·4H₂O, (3) [Cu(*o*-BMP)(H₂O)₂]·2H₂O, and (4) [Cd(*o*-BMP)(H₂O)₂]·2H₂O.

illustrated in Figures 3S–5S, and thermal decomposition steps are clarified in Schemes 6S–8S.

The TGA curve of [VO(*o*-H₂BMP)(SO₄)]·4H₂O validated five successive decomposition steps. An initial temperature range of 25–115 °C corresponds to the removal of four crystalline water molecules (weight loss: found 12.354%; calcd 12.245%). As a next step, the H₂SO₄ molecule was removed at 116–335 °C (weight loss: found 16.677%; calcd 16.665%). The third step occurred at 336–445 °C, which ascribed to the loss of C₇H₅NS moiety (weight loss: found 23.084%; calcd 22.972%). Fourth, a loss of C₇H₅N unit occurred between 446 and 535 °C (weight loss: found 17.075%; calcd 17.517%). The fifth step occurred at 536–800 °C, contributing to the loss of C₃H₃N₃O (weight loss: found 16.646%; calcd 16.50%). VO₂ is the final residue left behind after the complex decomposed entirely above 800 °C (remaining weight: found 14.136%; calcd 14.09%).

The TGA curve of [Cu(*o*-BMP)(H₂O)₂]·2H₂O demonstrated four decomposition stages. In the first step, two crystal water molecules were removed between 25 and 116 °C (weight loss: found 7.125%; calcd 7.40%). Second, both two coordinating water molecules accompanied by the C₅H₅N

moiety were lost at 117–309 °C (weight loss: found 23.258%; calcd 23.641%). The third step appeared at 310–419 °C and was attributed to C₇H₅NS loss (weight loss: found 27.652%; calcd 27.758%). In the last step, 420–800 °C was utilized for the loss of the C₅H₃N₃O fragment (weight loss: found 25.267%; calcd 24.867%), departing CuO as the final residue (remaining weight: found 16.698%; calcd 16.335%).

The TGA curve of [Cd(*o*-BMP)(H₂O)₂]·2H₂O revealed five decomposition steps. The first one was performed at 24–107 °C, which led to the removal of two crystal water molecules (weight loss: found 6.60%; calcd 6.724%). The next stage occurred at 108–333 °C and was attributed to the loss of two coordinating water molecules and the C₅H₅N moiety (weight loss: found 21.507%; calcd 21.485%). During the third step, the C₇H₅NS moiety was decomposed in the range 336–440 °C (weight loss: found 25.241%; calcd 25.230%). In step four, the remaining part of the organic skeleton, C₃H₃N₃O, was fired at a temperature range of 494–800 °C (weight loss: found 22.569%; calcd 22.60%), leaving CdO as final residual ash (remaining weight: found 24.082%; calcd 23.963%).

3.7.1. Kinetic and Thermodynamic Studies. TGA coupled with DTA diagrams were used to estimate kinetic and

Table 4. Crystallographic Data of *o*-H₂BMP Ligand and Its Metal Complexes

Compound	1	2	3	4
2θ	31.832	27.814	31.765	31.674
d -spacing (Å)	2.809	3.2037	2.8137	2.8215
fwhm (β)	0.100	0.100	0.113	0.100
crystal size (nm)	82.58	81.81	73.07	82.55
crystal system	triclinic	triclinic	monoclinic	monoclinic
cell parameters	$a = 8.3018 \text{ \AA}$, $b = 9.4214 \text{ \AA}$, $c = 16.2930 \text{ \AA}$, $\alpha = 83.450^\circ$, $\beta = 77.590^\circ$, $\gamma = 85.730^\circ$	$a = 7.9043 \text{ \AA}$, $b = 10.2300 \text{ \AA}$, $c = 12.5970 \text{ \AA}$, $\alpha = 102.320^\circ$, $\beta = 102.610^\circ$, $\gamma = 110.500^\circ$	$a = 8.2021 \text{ \AA}$, $b = 12.8425 \text{ \AA}$, $c = 14.6338 \text{ \AA}$, $\alpha = 90^\circ$, $\beta = 91.109^\circ$, $\gamma = 90^\circ$	$a = 6.8284 \text{ \AA}$, $b = 10.6888 \text{ \AA}$, $c = 18.5505 \text{ \AA}$, $\alpha = 90^\circ$, $\beta = 94.305^\circ$, $\gamma = 90^\circ$
cell volume	1234.81 \AA^3	883.04 \AA^3	1541.17 \AA^3	1350.13 \AA^3

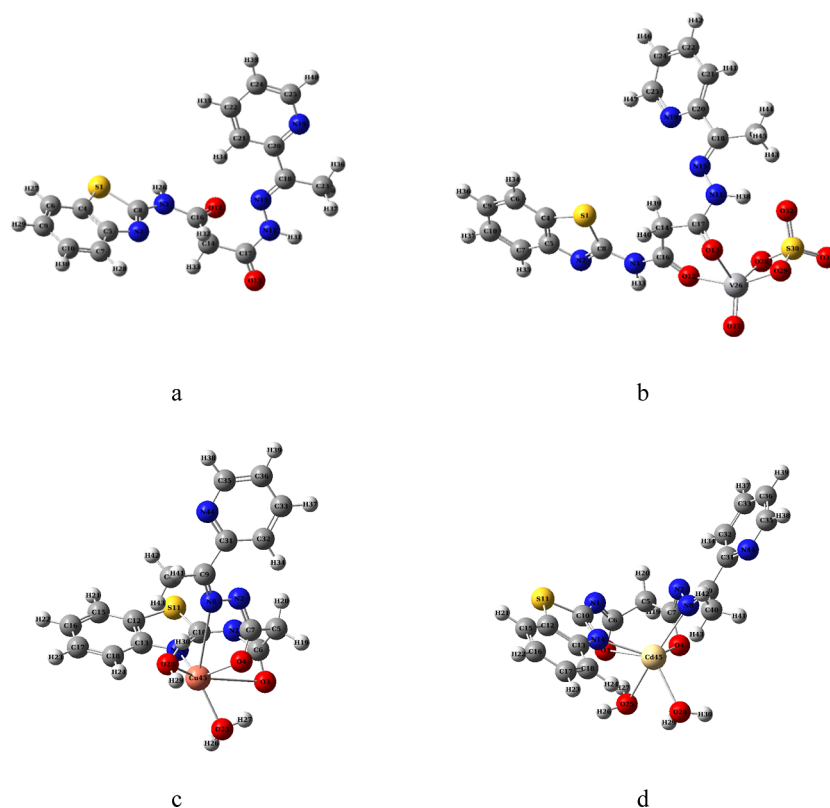


Figure 8. Molecular modeling of (a) *o*-H₂BMP, (b) [VO(*o*-H₂BMP)(SO₄)]·4H₂O, (c) [Cu(*o*-BMP)(H₂O)₂]·2H₂O, and (d) [Cd(*o*-BMP)(H₂O)₂]·2H₂O.

thermodynamic parameters using Coats–Redfern and Horowitz–Metzger methods,^{54–57} as shown in Figures 6S–11S. The calculated parameters (E_a , A , ΔH , ΔS , and ΔG) for the thermal degradation steps (Tables 4S–6S) can be concluded as follows: (i) the high activation energy (E_a) values for the thermal decomposition steps indicated the high stability of complexes;⁵⁸ (ii) all decomposition steps were endothermic processes as a result of ($+\Delta H$) enthalpy values; (iii) the ($+\Delta S$) entropy values indicated the fast decomposition reactions while the ($-\Delta S$) entropy values revealed the slow degradation stages;⁵⁹ (iv) the ($+\Delta G$) free energy values indicated that the free energy of the final residue is greater than that of the initial complex supporting the non-spontaneous processes.^{60–62}

3.8. PXRD Analysis. The PXRD analysis was done at room temperature via the Rigaku Ultima IV X-ray diffractometer with Cu anode radiation $K\alpha$ ($\lambda = 1.5418 \text{ \AA}$) and 2θ measuring from 4 to 70° . The prepared compounds showed diffraction patterns in Figure 7 analogues to crystalline phases natures. These patterns can be used to calculate the crystalline size (S)

at the most intense peak on the light of the Debye–Scherrer equation, $S = 0.9\lambda/(\beta \cos \theta)$, where $\lambda = 1.5406 \text{ \AA}$, β is the fwhm of the peak, and θ is the Bragg diffraction angle. Furthermore, the d -spacing values can be obtained by using the Bragg equation $n\lambda = 2d \sin(\theta)$, assuming ($n = 1$).⁶³ The PXRD data indexing analysis was performed by QualX software to determine the lattice parameters of the isolated compounds,⁶⁴ such as the crystal system, cell parameters, and cell volume, which are listed in Table 4. The indexing was established by comparing between 2θ values in the crystallography open database (COD)^{65–68} with the experimental data for isolated compounds, as illustrated in Table 7S.

The results revealed that the *o*-H₂BMP ligand and the VO(II) complex are polycrystalline with a triclinic crystal system, while both Cu(II) and Cd(II) complexes are polycrystalline within a monoclinic crystal system. The calculated crystal sizes were 82.58, 81.81, 73.07, and 82.55 nm, for the *o*-H₂BMP ligand, VO(II), Cu(II), and Cd(II)

Table 5. Calculated Dipole Moment, Total Energy, Binding Energy, and Chemical Reactivity Parameters^a

compound	1	2	3	4
dipole moment (<i>D</i>)	6.0221	18.0239	2.3230	5.605
<i>E</i> _{Total} (Hartree)	-1479.3152	-2325.0267	-1827.1159	-1679.0503
<i>E</i> _{binding} (Hartree)	–	-623.9644	-121.6967	-121.6791
<i>E</i> _{HOMO} (eV)	-0.2367	-0.2543	-0.2219	-0.2077
<i>E</i> _{LUMO} (eV)	-0.0698	-0.1052	-0.0639	-0.0736
<i>E</i> _{gap} (eV)	0.1669	0.1491	0.1580	0.1341
<i>χ</i> (eV)	0.1533	0.1798	0.1429	0.1407
<i>μ</i> (eV)	-0.1533	-0.1798	-0.1429	-0.1407
<i>η</i> (eV)	0.0835	0.0746	0.079	0.0671
<i>σ</i> (eV)	11.9832	13.4138	12.6582	14.9142
<i>ω</i> (eV)	0.1407	0.2167	0.1292	0.1475

^aNote: total energies of metals (V(IV), Cu(II), and Cd(II)) are -221.7474, -226.1040, and -78.0560 Hartree, respectively.

complexes, respectively. Whereas, the d-spacing result is 2.809, 3.2037, 2.8137, and 2.8215 nm, correspondingly.

3.9. Gaussian Studies. **3.9.1. Molecular Modeling.** DFT coupled with the [LANL2DZ/6-31G+(d,p)] mixed basis set^{69–72} was employed to optimize geometrically the molecular structure of all isolated compounds within atom numbering as represented in Figure 8. The results displayed in Table 8Sa,b showed that (i) the bond lengths of the most characteristic functional groups for isolated complexes correlate with the IR band expansions, confirming their participation in the coordination process, and (ii) the bond angles of the [Cu(*o*-BMP)(H₂O)₂].2H₂O and [Cd(*o*-BMP)(H₂O)₂].2H₂O complexes correlate a distorted octahedral arrangement, while the [VO(*o*-H₂BMP)(SO₄)]·4H₂O exists as a square-pyramidal geometry supporting the configurations concluded by UV–visible spectral analyses.⁷³

3.9.2. Frontier Molecular Orbitals and Molecular Chemical Parameters. As a complement to the conceptual density functional theory calculations, the dipole moment (*D*) and distinct quantum energetic values have been derived as represented in Table 5, such as the total electronic energies (*E*_{Total}) and the complex binding energy (*E*_{binding}).⁷⁴ Furthermore, the energies of frontier molecular orbitals (*E*_{HOMO} and *E*_{LUMO}) which are subjected to calculation (*E*_{gap}) as well as several global and local descriptors of chemical reactivity like the electronegativity (*χ*), the chemical potential (*μ*), the hardness (*η*), the softness (*σ*), and the electrophilicity index (*ω*)⁷⁵ are presented in eqs 11–17.

$$E_{\text{binding}} = E_{\text{complex}} - E_{\text{metal}} - E_{\text{ligand}} \quad (11)$$

$$E_{\text{gab}} = E_{\text{LUMO}} - E_{\text{HOMO}} \quad (12)$$

$$\chi = -(E_{\text{LUMO}} + E_{\text{HOMO}})/2 \quad (13)$$

$$\mu = -\chi = (E_{\text{LUMO}} + E_{\text{HOMO}})/2 \quad (14)$$

$$\eta = (E_{\text{LUMO}} - E_{\text{HOMO}})/2 \quad (15)$$

$$\sigma = 1/\eta^- \quad (16)$$

$$\omega = \mu^2/2\eta \quad (17)$$

The frontier molecular orbital distribution of the compounds is depicted in Figure 9. The low values of the HOMO and LUMO energy gaps showed that the studied compounds have high chemical reactivity, biological activity, and polarizability. Chemical potential is used to determine the stability of isolated compounds. It can also predict their tendency to

chemically react to form new substances, transform into new physical states, or migrate from one spatial location to another.^{76,77} Both chemical potential energy and electronegativity can also be thought of as depending on chemical composition, where the VO(II) complex possesses the most negative chemical potential magnitude (*μ* = -0.1798) and the largest electronegativity value (*χ* = 0.1798) among the compounds, enhancing the lowest stability or the most reactivity.

The free ligand is the hardest (lowest soft) base compound with values (*η* = 0.0835, *σ* = 11.9832) as a result of bearing the greatest number of highly electronegative donor atoms (O or N centers). This refers to the steadiness of prepared complexes using such hydrazone ligands, where generally the stable complexes are formed between hard acids and hard bases or between soft acids and soft bases. Based on the minimum electrophilicity principle stated as “Electrophilicity will be a minimum (maximum) when both chemical potential and hardness are maxima (minima)”, the order of the compounds according to their electrophilicity index (*ω*) is VO(II) complex > Cd(II) complex > ligand > Cu(II) complex.

3.9.3. Molecular Electrostatic Potential. The molecular electrostatic potential (MEP) is used to predict the relative reactivity positions in a species for nucleophilic and electrophilic attack and to study the hydrogen bonding interactions, in addition to evaluating some biological significance. The MEPs of the optimized geometry of the *o*-H₂BMP ligand and its complexes were obtained based on their DFT calculation.⁷⁸

The MEP mapping for an isolated ligand and its complexes can be categorized into three zones according to their colors, as shown in Figure 10: (i) the red region matches the high electronic density zone, which enhances the electrophilic attack interactions; (ii) the green region indicates the neutral electrostatic potential zone; and (iii) the blue region refers to the low electronic density zone, which reflects the nucleophilic attack demeanor.⁷⁹

As can be seen for compound 1, the negative electrostatic potential regions are localized over the electronegative atoms (**O**-carbonyl groups, **S**-thiazole ring, **N**-thiazole ring, **N**-Schiff base moiety, and **N**-pyridine ring), while the positive electrostatic potential regions are mainly centered over hydrogen atoms of **NH**-imine groups. Also, compound 2 has negative electrostatic potential regions focused over the sulfate group and oxovanadium species, causing a strong effect in different interactions. On the other hand, both compounds 3 and 4 have weak negative electrostatic potential regions limited

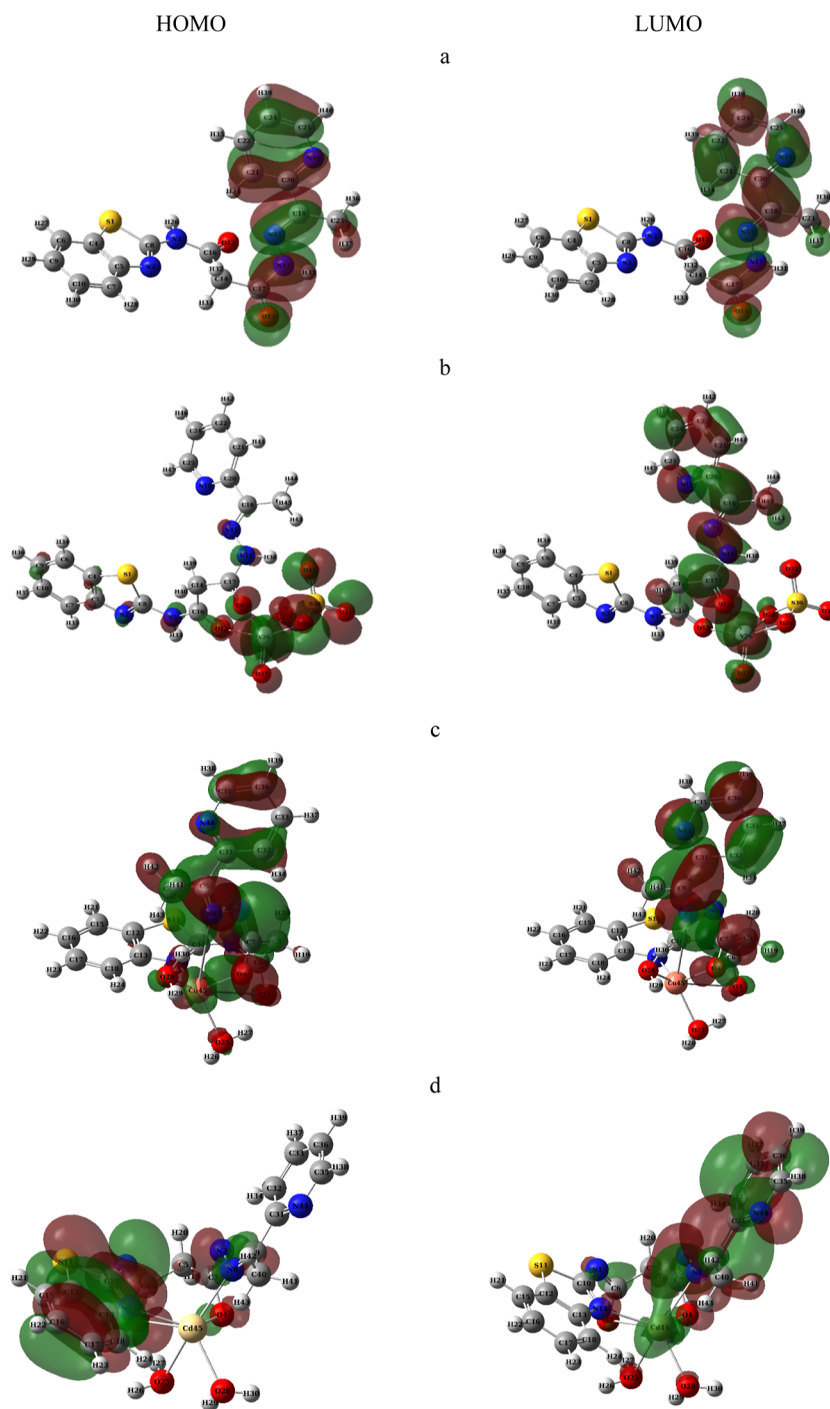
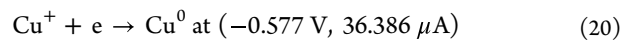
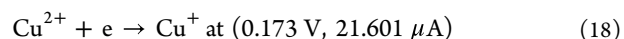


Figure 9. HOMO and LUMO of (a) *o*-H₂BMP, (b) [VO(*o*-H₂BMP)(SO₄)]·4H₂O, (c) [Cu(*o*-BMP)(H₂O)₂]·2H₂O, and (d) [Cd(*o*-BMP)(H₂O)₂]·2H₂O.

to pyridine nitrogen within intense positive electrostatic potential regions over hydrogen atoms of water molecules.

3.10. Cyclic Voltammetry. **3.10.1. CV of Cu(II).** The electrochemical behavior of 3.13×10^{-3} M of Cu(II) cation was studied via CV using a glassy carbon working electrode immersed in 0.1 M of supporting electrolyte KCl dissolved in a 50% DMSO–50% water mixed solvent. The scanning was applied at a potential window (1.2 to -1.2 V) within a 0.1 V/s scan rate at 291.15 K, as shown in Figure 11. The voltammogram showed two peaks in the reduction sweeping and two in the oxidation side, corresponding to the

conversions between [Cu(II)/Cu(I)], [Cu(I)/Cu(0)] species. The mechanisms of both reduction and oxidation reactions can be described as follows



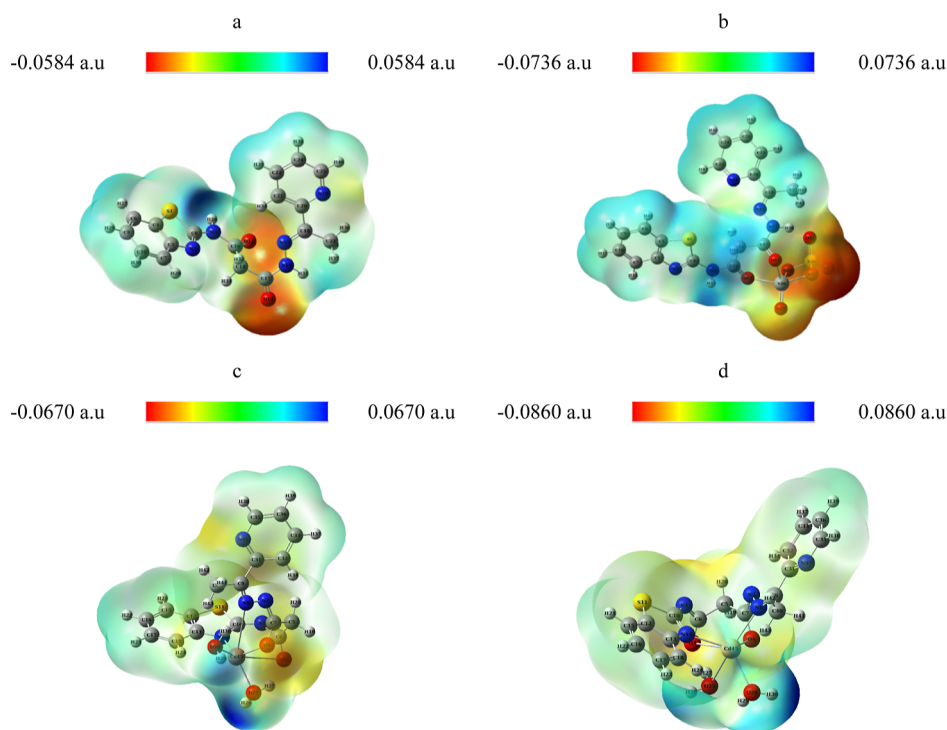


Figure 10. MEP surface maps of (a) *o*-H₂BMP, (b) [VO(*o*-H₂BMP)(SO₄)]·4H₂O, (c) [Cu(*o*-BMP)(H₂O)₂]·2H₂O, and (d) [Cd(*o*-BMP)(H₂O)₂]·2H₂O.

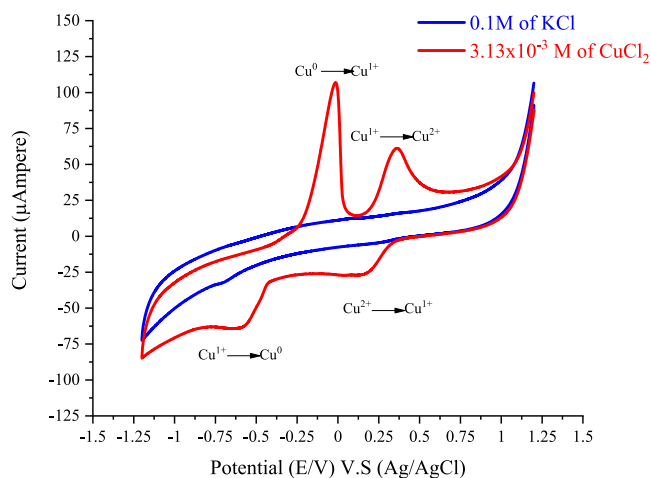


Figure 11. CV of 3.13×10^{-3} M Cu(II) in 0.1 M KCl.

3.10.2. CV of the Cu (II)/*o*-H₂BMP System. The electrochemical behavior for the complexation reaction between *o*-H₂BMP and copper species was studied with the same conditions and settings as shown in Figure 12. The voltammogram revealed the interaction between copper and ligand species according to the potential shifts to new values and the decreases in both cathodic and anodic peak currents.

Also, the stability constants (β_j), a measure of the strength of the interaction between the metal ion and ligand to form the complex, can be evaluated by Lingane's eq 22⁸⁰

$$\begin{aligned} \Delta E^\circ &= E_C^\circ - E_M E_M^\circ \\ &= -(2.303RT/nF) \log \beta_j - (2.303RT/nF) j \log [L] \end{aligned} \quad (22)$$

where both E_C° and E_M° are the formal peak potentials corresponding to the complex and free metal ions, n is the number of electrons, F is the Faraday constant (96,485.33 Coulomb/mol), R is a gas constant (8.314 J mol⁻¹ K⁻¹), T is the absolute temperature, j is the molar ratio of the stoichiometric complex, and $[L]$ is the *o*-H₂BMP ligand concentration. The formal potential (E°) was determined as follows

$$E^\circ = (E_a + E_c)/2 \quad (23)$$

By plotting $-\log [L]$ versus ΔE° ⁸¹ as shown in Figure 13 on the aid of (E_{pc} , E_{pa} , i_{pa} , i_{pc} , E° , j) data present in Table 6, the value of j calculated from the slope was achieved ($0.9497 \approx 1$), as explained in eq 24

$$\text{slope} = (2.303RT/nF)j \quad (24)$$

Further, on plotting (j) values versus (i_{pa}) anode peak current in the (Cu⁺ to Cu²⁺) peak, the break on the curve ($j = 1.04 \approx 1$) predicts (1:1) stoichiometry as shown in Figure 14, which coincided with the results from the elemental analysis calculations.

The stability constant was achieved ($\beta_j = 28.18 \times 10^3$, $\log \beta_j = 4.45$), and the Gibbs free energy was obtained ($\Delta G = -24.80$ kJ/mol) based on the eq 25,⁸² predicting a favorable (1:1) stable and spontaneous interaction between Cu²⁺ and *o*-H₂BMP species in the solution environment.

$$\Delta G = -2.303RT \log \beta_j \quad (25)$$

3.11. Biological Studies. 3.11.1. Antioxidant Studies. The antioxidant capacity of the (*o*-H₂BMP) ligand and its complexes were measured using DPPH and ABTS radical scavenging methods, and usually, L-ascorbic acid (Vitamin C) is utilized as a reference.⁸³ The percentage of inhibition was obtained from eq 26

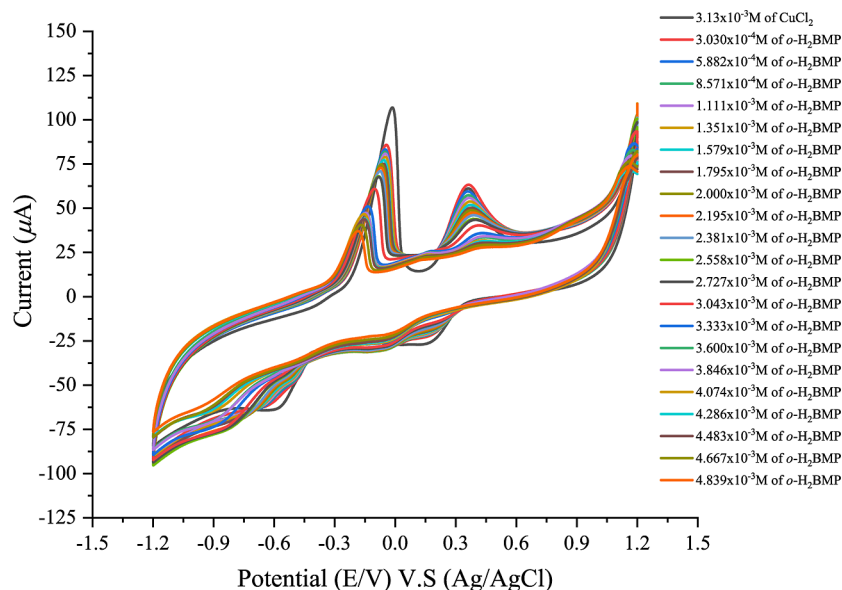


Figure 12. CV of 3.13×10^{-3} M Cu(II) in 0.1 M KCl in the presence of *o*-H₂BMP.

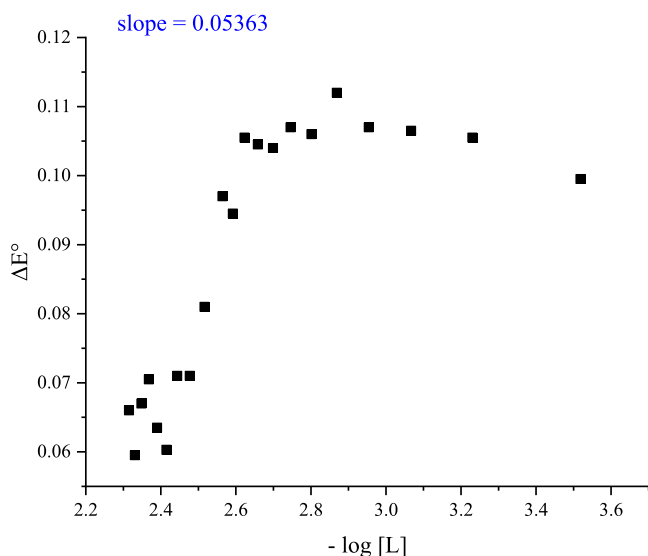


Figure 13. Plot of $-\log[L]$ vs ΔE° .

$$\text{inhibition effect (I \%)} = \frac{\text{Abs}_{\text{control}} - \text{Abs}_{\text{sample}}}{\text{Abs}_{\text{control}}} \times 100 \quad (26)$$

The concentrations 370.37 and 250 μM were used to obtain the optimum inhibition effect in both the DPPH and ABTS methods, respectively. The free ligand and complexes displayed DPPH antioxidant activity in the sequence: (5.10%; Cd(II) complex) < (23.40%; *o*-H₂BMP) < (43.90%; Cu(II) complex) < (87.31%; VO(II) complex), while displayed ABTS antioxidant activity in the sequence: (33.66%; Cu(II) complex) < (92.98%; Cd(II) complex) < (94.93%; *o*-H₂BMP) < (95.09%; VO(II) complex) as illustrated in Figure 15. The IC₅₀ values were calculated for the samples that gave (I %) of more than (50%) by using the serial dilutions (370, 185, 92.5, 46.25, and 23.125 μM for DPPH) and (250, 125, 62.5, 31.25, and 15.625 μM for ABTS) and then plotting the values of the ordered concentrations versus inhibition percent via the

GraphPad Prism 9 program, as shown in Figures 12S and 13S and listed in Tables 7, 9S, and 10S.

3.11.2. Microbial Studies. The antimicrobial activity index of (*o*-H₂BMP) ligand and metal complexes compared to gentamycin and clotrimazole standards can be evaluated⁸⁴ by using eq 27

$$\begin{aligned} & \% \text{ antimicrobial activity} \\ &= \frac{\text{inhibitory zone for sample (mm)}}{\text{inhibitory zone for standard (mm)}} \times 100 \end{aligned} \quad (27)$$

The screening, as summarized in Table 8, reflects the following results: (i) the antimicrobial activity for the ligand revealed remarkable values in the range between (65.0–71.4%) compared to the standards against all microbial strains except *S. typhi* (ii) copper complex showed moderate values between (39.4–60.0%) against all strains excluding *S. typhi* (iii) cadmium complex gave values close to 40% with Gram-positive bacteria and fungus whereas inactive toward Gram-negative bacteria (iv) oxovanadate complex inhibited *B. subtilis* with 54.2% and *S. typhi* with 56.2% only.

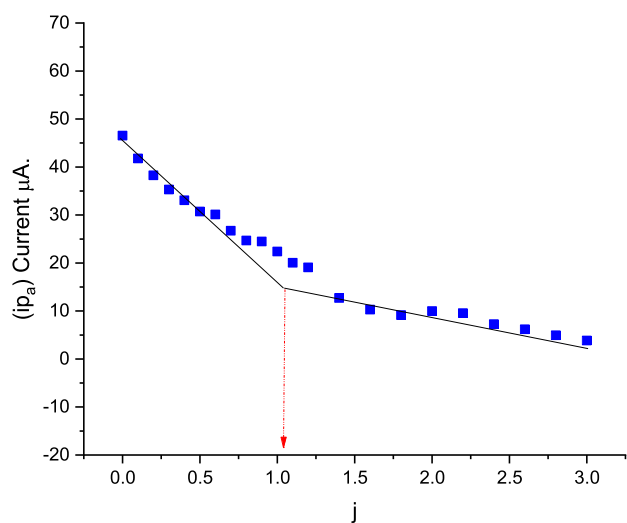
3.11.3. Cell Viability. The synthesized ligand, metal complexes, and the corresponding free metal salts were assessed via the MTT assay against MDA-MB-231 and MCF-7 breast cancer cells on the use of *cis*-platin as a positive control. This method depends on the conversion of the yellow tetrazolium bromide (MTT) by mitochondrial succinate dehydrogenase in viable cells to a purple formazan derivative, which can be measured spectrophotometrically, and the percent of cell viability was calculated using eq 28^{85–87}

$$\text{cell viability} = \frac{\text{mean absorbance of treated}}{\text{mean absorbance of untreated}} \times 100 \quad (28)$$

In order to determine the IC₅₀, the cells were incubated with serial dilutions (50, 25, 12.5, 6.25, 3.125, and 1.56 μM) of the most active compounds which gave cell viability less than 50%, and plotted the ordered concentrations of each compound (conc.) against the percentage of cell viability (% cell viability)

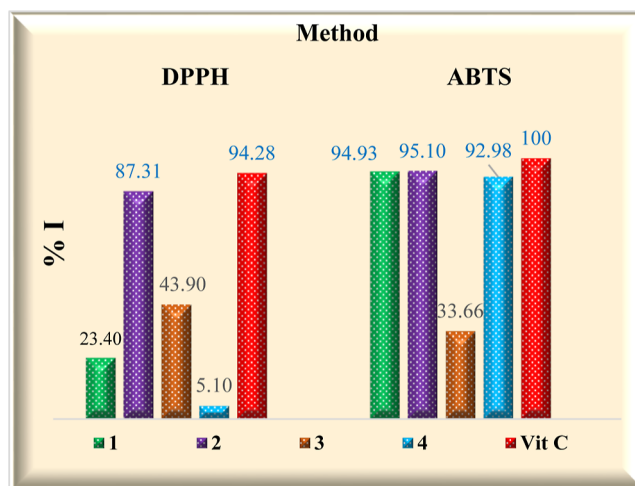
Table 6. CV Data of CuCl₂ (Cu²⁺/Cu⁺) in the Absence and Presence of (*o*-H₂BMP) Ligand at 291.15 K

$M \times 10^{-3}$ CuCl ₂	$M \times 10^{-3}$ <i>o</i> -H ₂ BMP	E_{pa} (V)	E_{pc} (V)	i_{pa} (μ A)	i_{pc} (μ A)	E° (V)	ΔE° (V)	j
3.13		0.357	0.173	46.537	21.601	0.265		0
3.03	0.3030	0.357	-0.026	41.780	17.748	0.1655	0.100	0.1
2.94	0.5882	0.353	-0.034	38.257	18.545	0.1595	0.106	0.2
2.86	0.8571	0.354	-0.037	35.294	18.829	0.1585	0.107	0.3
2.78	1.111	0.358	-0.042	33.069	18.572	0.158	0.107	0.4
2.70	1.351	0.362	-0.056	30.712	18.499	0.153	0.112	0.5
2.63	1.579	0.365	-0.047	30.095	17.945	0.159	0.106	0.6
2.56	1.795	0.366	-0.05	26.730	17.170	0.158	0.107	0.7
2.50	2.000	0.37	-0.048	24.689	17.477	0.161	0.104	0.8
2.44	2.195	0.371	-0.05	24.474	17.715	0.1605	0.105	0.9
2.381	2.381	0.365	-0.046	22.385	17.271	0.1595	0.106	1
2.33	2.558	0.374	-0.033	20.052	15.228	0.1705	0.095	1.1
2.27	2.727	0.378	-0.042	19.078	15.814	0.168	0.097	1.2
2.17	3.043	0.397	-0.029	12.721	15.312	0.184	0.081	1.4
2.08	3.333	0.402	-0.014	10.285	12.994	0.194	0.071	1.6
2.00	3.600	0.404	-0.016	9.1415	11.326	0.194	0.071	1.8
1.92	3.846	0.41	-0.006	9.9837	10.948	0.2047	0.060	2
1.85	4.074	0.41	-0.007	9.5524	7.9592	0.2015	0.064	2.2
1.79	4.286	0.405	-0.016	7.2598	9.9597	0.1945	0.071	2.4
1.72	4.483	0.407	-0.011	6.1943	8.6621	0.198	0.067	2.6
1.67	4.667	0.405	0.006	4.9333	8.9457	0.2055	0.060	2.8
1.61	4.839	0.402	-0.004	3.8367E	8.3597	0.199	0.066	3

Figure 14. Plot of j vs i_{pa} .

as described in Figures 16, 14S, and 15S and listed in Tables 9, 11S, and 12S.

According to the results, which reflect the ability to reduce the growth of (MDA-MB-231) and (MCF-7) tumor cells, the tested compounds can be discussed as follows: (i) low toxic compounds within high cell viability percentages (>50%) appear on both the free ligand (56.4% against MDA-MB-231 and 85.2% against MCF-7) and the Cu(II) complex (86.6% against MDA-MB-231 and 71.1% against MCF-7), (ii) all metal salts VO(SO₄), CuCl₂, and CdCl₂ can be considered as high toxic compounds accompanied by low cell viability values against both breast cancer cell lines, (iii) the most toxic compounds with no substantial cell viability is Cd(II) complex predominantly, (iv) VO(II) complex is the most compatible compound with *cis*-platin where it gave a noticeable cell viable percent (10.9%) against (MCF-7) tumor cells without any viability against (MDA-MB-231) cells. Further, the largest IC₅₀

Figure 15. Inhibition effect (I %) values of the DPPH and ABTS methods.Table 7. Results of (I %) and IC₅₀ by DPPH and ABTS Methods

no.	DPPH method		ABTS method	
	I %	IC ₅₀ (μ M)	I %	IC ₅₀ (μ M)
1	23.4	—	94.9	23.09
2	87.3	21.8	95.1	6.3
3	43.9	—	33.7	—
4	5.1	—	93.0	58.6
Vit C	94.3	27.8	100	3.6

values were found for the Cd(II) complex and CuCl₂, which were highly effective against MDA-MB-231 (10.5 and 10.9 μ M) and MCF-7 (7.3 and 7.2 μ M). However, against MDA-MB-231, the smallest IC₅₀ values were achieved with the VO(II) complex (4.5 μ M) and VO(SO₄) (4.4 μ M), while against

Table 8. Results of the Inhibitory Zone and the % Antimicrobial Activity for *o*-H₂BMP and Its Metal Complexes

no.	bacterial strains				
	Gram-positive bacteria		Gram-negative bacteria		fungus
	<i>S. aureus</i>	<i>B. subtilis</i>	<i>E. coli</i>	<i>S. typhi</i>	<i>Candida</i>
1	15 mm, (71.4%)	17 mm, (70.8%)	13 mm, (65%)	–	23 mm, (69.7%)
2	–	13 mm, (54.2%)	–	9 mm, (56.25%)	–
3	10 mm, (47.6%)	10 mm, (41.7%)	12 mm, (60%)	–	13 mm, (39.4%)
4	10 mm, (47.6%)	11 mm, (45.8%)	–	–	14 mm, (42.4%)
gentamicin	21 mm, (100%)	24 mm, (100%)	20 mm, (100%)	16 mm, (100%)	–
clotrimazole	–	–	–	–	33 mm, (100%)

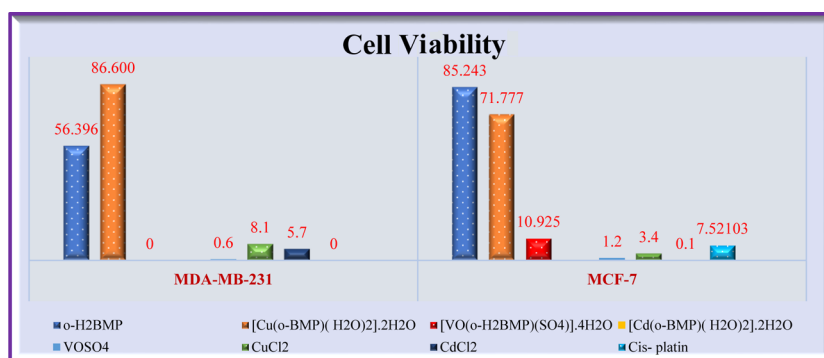


Figure 16. Percentage cell viability of MDA-MB-231 and MCF-7 cell lines.

Table 9. Results of % Cell Viability and IC₅₀ of MDA-MB-231 and MCF-7 Cell Lines

no.	MDA-MB-231		MCF-7	
	% cell viability	IC ₅₀ (μM)	% cell viability	IC ₅₀ (μM)
<i>o</i> -H ₂ BMP	56.3	–	85.2	–
[VO(<i>o</i> -H ₂ BMP)(SO ₄) ₂].4H ₂ O	0	4.5	10.9	6.8
[Cu(<i>o</i> -BMP)(H ₂ O) ₂].2H ₂ O	86.6	–	71.7	–
[Cd(<i>o</i> -BMP)(H ₂ O) ₂].2H ₂ O	0	10.5	0	7.2
VOSO ₄	0.6	4.3	1.2	5.9
CuCl ₂	8.1	10.9	3.4	7.1
CdCl ₂	5.7	8.1	0.1	2.5
cisplatin	0	7.2	7.5	31.4

MCF-7, the smallest IC₅₀ values were achieved with CdCl₂ (2.5 μM) and VOSO₄ (5.9 μM).

As a consequence of the above remarks, the metal complexes and their corresponding metal salts showed better cytotoxic potency and lower cell viability than the free ligand and comparable potency to that of *cis*-platin. Specifically, one of the VO(II) complexes from the series presented great cytotoxic activity against all cancer cell lines that were tested in this study, with IC₅₀ values in the range of 4.5–6.8 μM.

3.12. Molecular Docking. The main factor responsible for breast cancer development is estrogen. In many breast cancers, alpha estrogen receptor (ER_α) activation increases cancer proliferation, while beta estrogen receptor (ER_β) activation inhibits it.^{88,89}

In this research, the molecular docking of the novel (*o*-H₂BMP) ligand and its complexes as human ER_α inhibitors within protein or enzyme receptors (6CBZ, 1FDW, 2WTT, 4GL7, 1A53, and 1X7R) were studied. The results of the binding energy scores (S), bond energy, total energy, types of

bonds, types of interactions, and root-mean-square deviation (rmsd) collected in Table 10 showed a high degree of

Table 10. Most Efficient Docking Results of the (*o*-H₂BMP) Ligand and Its Complexes

no.	enzyme (PDB code)	S	rmsd	no. of bonds	total energy (kcal/mol)
1	1A53	−7.7177	1.399	2	−10.9
1	2WTT	−5.7477	1.8404	4	−9.2
1	6CBZ	−5.3872	1.181	1	−8.8
2	4GL7	−7.8116	1.2756	8	−27
2	6CBZ	−6.0583	1.7843	3	−16.2
2	2WTT	−5.6126	1.4855	5	−12
2	1A53	−6.1172	2.6850	7	−12.1
2	1X7R	−6.811	1.6811	6	−10.3
3	1A53	−6.4602	2.684	9	−29.6
3	2WTT	−5.3431	2.6696	2	−11.1
3	1X7R	−4.6324	0.9098	4	−10.7
4	1A53	−5.7249	1.3188	7	−27.7
4	1X7R	−3.7207	1.4272	5	−16.5
4	1FDW	−5.3399	2.4339	3	−12.5

selectivity and potency toward binding to the active sites of the proteins being studied. Molecular docking studies identify various types of interactions, such as hydrophobic, electrostatic, and H-bonding.^{90,91}

The most efficient docking results represented in Table 10 revealed the following observations: (i) compound 1 predicted the highest total energy value (−10.9 kcal/mol) toward the protein receptors pocket (1A53) where this free ligand interacted with (LYS53) and (ARG182) amino acids via ligand active centers (O18 and O19) producing two hydrogen bonds as shown in Figures 17 and 18, also (ii) compound 2 predicted the largest total energy value (−27 kcal/mol) where this complex interacted through seven hydrogen bonds and

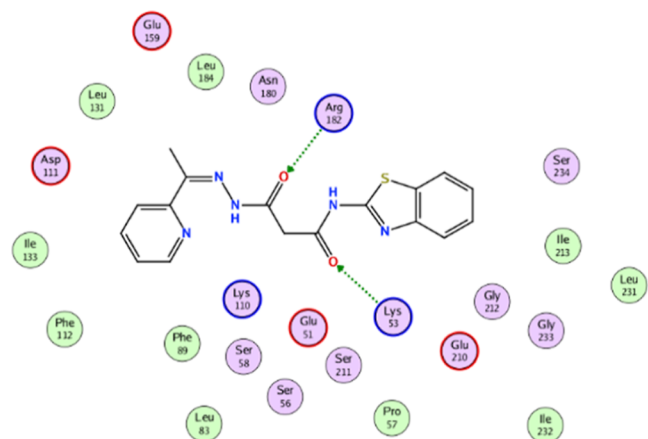


Figure 17. 2D interaction between (*o*-H₂BMP) and 1A53.

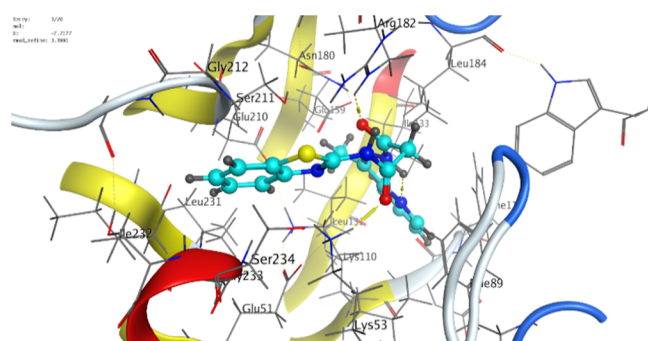


Figure 18. 3D interaction between (*o*-H₂BMP) and 1A53.

one ionic bond with six amino acids (MET303, GLY436, ARG115, ARG435, TRP141, and ARG145) as illustrated in Figures 19 and 20, as well (iii) compound 3 predicted the best total energy value (-29.6 kcal/mol) toward the protein receptors pocket (1A53) where this complex interacted by three conventional hydrogen bonds, one ionic, one π -cation, and four π -H interactions, with six amino acids (SER211, LYSS3, ARG182, ASN180, GLY212, and SER234) as clarified in Figures 21 and 22, finally (iv) compound 4 predicted the

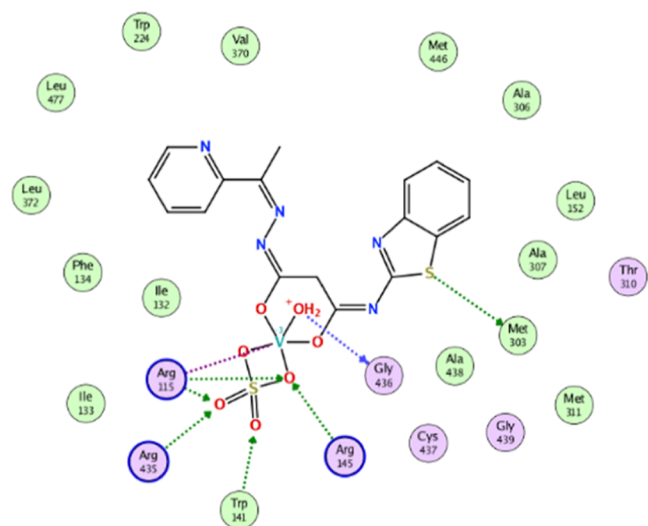


Figure 19. 2D interaction between $[\text{VO}(\text{o-H}_2\text{BMP})(\text{SO}_4)] \cdot 4\text{H}_2\text{O}$ and 4GL7.

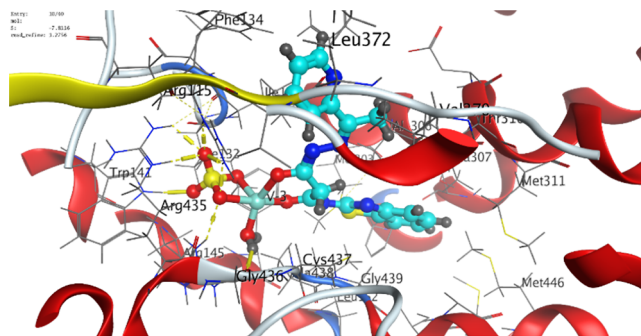


Figure 20. 3D interaction between $[\text{VO}(\text{o-H}_2\text{BMP})(\text{SO}_4)] \cdot 4\text{H}_2\text{O}$ and 4GL7.

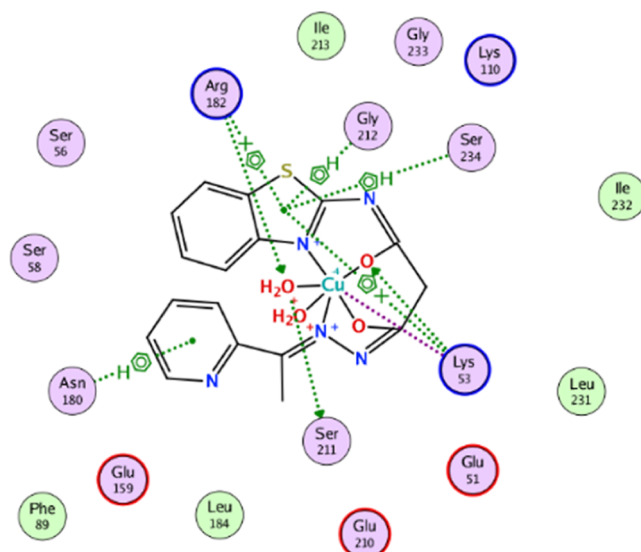


Figure 21. 2D interaction between $[\text{Cu}(\text{o-BMP})(\text{H}_2\text{O})_2] \cdot 2\text{H}_2\text{O}$ and 1A53.

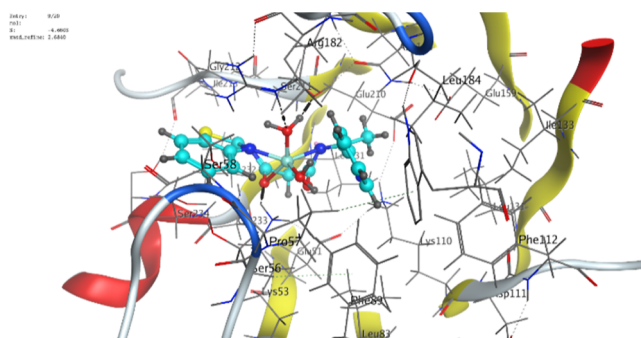


Figure 22. 3D interaction between $[\text{Cu}(\text{o-BMP})(\text{H}_2\text{O})_2] \cdot 2\text{H}_2\text{O}$ and 1A53.

highest total energy value (-27.7 kcal/mol) toward the protein receptors pocket (1A53) where this complex interacted by three conventional hydrogen bonds, one ionic, one π -cation, and two π -H interactions, with four amino acids (SER211, LYSS3, ARG182, and SER234) as represented in Figures 23 and 24. More details about the molecular docking study are mentioned in Supporting Information, Tables 13S–18S and Figures 16S–27S.

According to the docking results, it can be concluded that the complexes of $[\text{VO}(\text{o-H}_2\text{BMP})(\text{SO}_4)] \cdot 4\text{H}_2\text{O}$ and $[\text{Cd}(\text{o-BMP})(\text{H}_2\text{O})_2] \cdot 2\text{H}_2\text{O}$ are efficient as anticancer, which are so

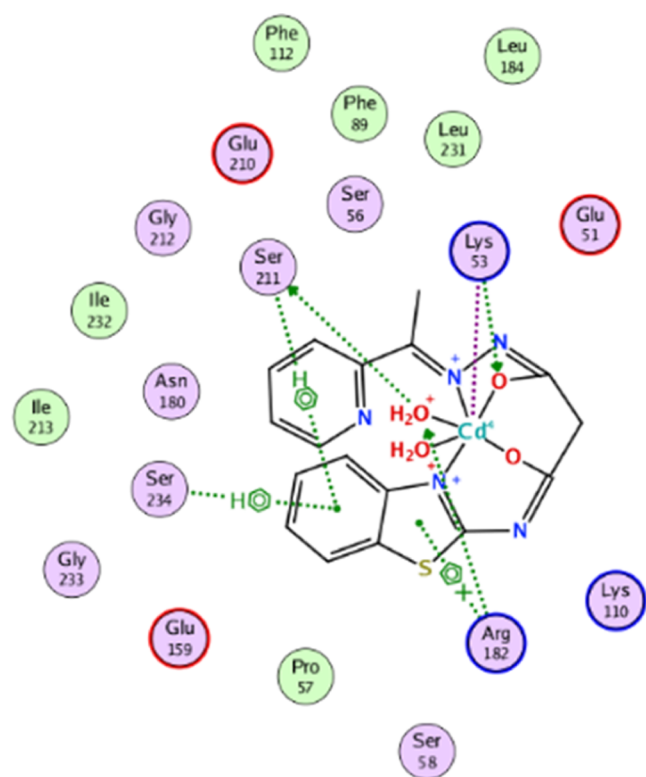


Figure 23. 2D interaction between $[\text{Cd}(\text{o-BMP})(\text{H}_2\text{O})_2]\cdot 2\text{H}_2\text{O}$ and 1A53.

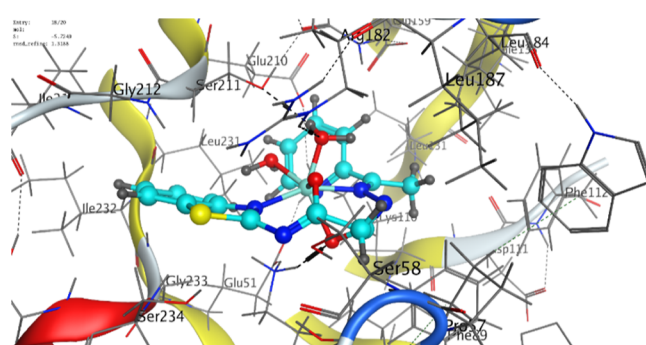


Figure 24. 3D interaction between $[\text{Cd}(\text{o-BMP})(\text{H}_2\text{O})_2]\cdot 2\text{H}_2\text{O}$ and 1A53.

closely matched with the experimental cytotoxicity screening on both cell lines (MDA-MB-231) and (MCF-7). The MEPs give us useful information about the potent sites concerning the interactions with the residues present in amino acids of protein receptors via hydrogen bonds. Where the H-acceptor interaction in molecular docking coincides with the red regions in MEP surface maps enhancing nucleophilic attack, whereas the H-donor interaction corresponds to the blue regions in MEP surface maps enhancing electrophilic attack.

3.13. Structure–Activity Relationship Studies. Many parameters like the dipole moment, E_{HOMO} , E_{LUMO} , and E_{gap} , which depend on the theoretical data of DFT calculations, can be linked to the antimicrobial and antioxidant activity of compounds under study through the structure–activity relationship (SAR)⁹² as dipole moments are very useful in determining penetration rates through cell membranes and excretion rates. The studies of SAR predicted an inverse relationship between the dipole moment and the activity of

compounds against the examined microorganism. With a reduced dipole moment, the compound becomes more lipophilic, which allows better penetration through the lipid layer of microorganisms, thus damaging them quickly. Based on the outcome data, the VO(II) complex exhibited a higher dipole moment than other complexes and caused the lowest antimicrobial activity. Whereas the free ligand, which contains donor atoms such as oxygen, nitrogen, and sulfur atoms that can donate electrons to biological receptors, has a low dipole moment, so the free ligand is more active as the bactericidal and fungicidal agent. In general, the lower results as antimicrobial agents are ascribed to their inability to diffuse through the microorganism lipid layer due to the dipole moment increasing.^{93,94}

The E_{HOMO} and E_{LUMO} are closely concerned with the free radical scavenging activity of the antioxidant agents. In concept, nucleophiles and electrophiles share radical scavenging activities endorsed by the relative energy influence of the HOMO/LUMO orbitals, where the substance has a low E_{gap} , loses electrons more easily, and thus, it can participate in reactions. All investigated compounds that have low E_{gap} values have been classified as good electron-releasing species with potent antioxidant activity.^{95,96} Particularly, the VO(II) complex showed the greatest antioxidant efficiency toward both DPPH ($I = 87.3\%$, $\text{IC}_{50} = 21.8 \mu\text{M}$) and ABTS ($I = 95.1\%$, $\text{IC}_{50} = 6.3 \mu\text{M}$).

3.14. Molecular Property and Drug-Likeness Prediction. The hydrazone (*o*-H₂BMP) ligand and its complexes were examined to check their compatibility with the Lipinski rule of five,^{97–99} according to which an orally active drug has no more than one violation of the following criteria: hydrogen bond donors (HBD: the total number of nitrogen–hydrogen and oxygen–hydrogen bonds) ≤ 5 , hydrogen bond acceptors (HBA: all nitrogen or oxygen atoms) ≤ 10 , an octanol–water partition coefficient ($\log P$) ≤ 5 , and molecular weight (m. wt) ≤ 500 . Molecular weight is very influential for drugs that interact with drug receptors/DNA. As the molecular weight increases, the compounds become denser. As well, $\log P$ values play a major role in promoting inactive membrane division and activating permeability, in the opposite direction of their influence on solubility. Finally, polar surface atoms (PSA) such as nitrogen, oxygen, and sulfur are significant parameters to evaluate drug transport properties. Based on MolSoft software, a model for estimating the drug-likeness score of the investigated compounds and their molecular properties was developed and summarized in Table 11. The values of HBA and HBD for most compounds obey the applied rule, so the prepared compounds could implement through the cellular membrane and acting as drugs.

Table 11. Calculated Parameters for Drug-Likeness Based on the Lipinski Rule^a

no.	m. wt	$\log P$	HBA	HBD	PSA	m. volume
1	353.41	1.76	7	2	96.34	301.24
2	516.41	−2.4	12	2	154.22	383.6
3	450.97	−5.9	9	4	109.74	341.03
4	499.83	−5.9	9	4	109.74	341.03

^aNotes: HBA and HBD are hydrogen bond acceptors and hydrogen bond donors, respectively. The calculated m.wt of compounds does not include crystallized water molecules.

4. CONCLUSIONS

A series of Cu(II), VO(II), and Cd(II) metal complexes were prepared using a novel hydrazone ligand (*o*-H₂BMP). These synthesized compounds were structurally characterized through several spectroscopic techniques, which revealed that the ligand behaved either neutral bidentate with VO(II) or bidentate tetradentate with Cu(II) and Cd(II). Electronic spectra as well as magnetic measurements suggested the octahedral configurations for Cu(II) and Cd(II); while the square pyramidal around the VO(II) ion. PXRD patterns referred that all compounds had crystal phase characteristics and crystal size within the nanoscale range. Moreover, the Qualx calculations related to the X-ray diffraction patterns showed that both the free ligand and the vanadium complex have a triclinic crystal system, while the copper and cadmium complexes have a monoclinic crystal system. As well, the compounds are computationally simulated using Gaussian 09 view via B3LYP functional and LANL2DZ/6-31+G(d,p) mixed basis set to predict the optimized structures. The DFT calculations reveal that all isolated compounds are chemically and biologically active. In addition, the electrochemical measurements performed for Cu(II) in absence/presence of ligand showed the formation of a (1:1) stable complex through a spontaneous process. Finally, the outcome data from biological activities for the all-isolated solid compounds were screened practically through antioxidant, antimicrobial, and cytotoxicity studies and screened theoretically using MOE docking, SAR, and drug-likeness prediction. The antioxidant activity of the VO(II) complex is more potent than Vit C in the DPPH method. Also, the antimicrobial activity values for the *o*-H₂BMP ligand and its complexes (100 mL) revealed good activity compared to the gentamicin standard against *B. subtilis*. Finally, the IC₅₀ values of VO(II) and Cd(II) complexes showed high performance in MDA-MB-231 and MCF-7, respectively.

■ ASSOCIATED CONTENT

Supporting Information

The Supporting Information is available free of charge at <https://pubs.acs.org/doi/10.1021/acsomega.2c07592>.

Biological screening method, IR correlation data, ¹H NMR data, TGA curves, DFT calculations, molecular docking, and other supporting data (PDF)

■ AUTHOR INFORMATION

Corresponding Author

Anwer G. Al-Harazie – Chemistry Department, Faculty of Education and Applied Sciences—Arhab, Sana'a University, Sana'a 1247, Yemen; Chemistry Department, Faculty of Science, Mansoura University, Mansoura 35511, Egypt;
orcid.org/0000-0002-2849-3391;
Email: alharazie2012@gmail.com, a.alharazie@su.edu.ye

Authors

Esam A. Gomaa – Chemistry Department, Faculty of Science, Mansoura University, Mansoura 35511, Egypt
Rania R. Zaky – Chemistry Department, Faculty of Science, Mansoura University, Mansoura 35511, Egypt
Mahmoud N. Abd El-Hady – Chemistry Department, Faculty of Science, Mansoura University, Mansoura 35511, Egypt

Complete contact information is available at:

<https://pubs.acs.org/10.1021/acsomega.2c07592>

Author Contributions

The manuscript was written through the contributions of all authors. All authors have given approval to the final version of the manuscript.

Notes

The authors declare no competing financial interest.

■ ACKNOWLEDGMENTS

This work was supported by the Chemistry Department, Faculty of Education and Applied Sciences—Arhab, Sana'a University, Yemen, and the Department of Chemistry, Faculty of Science, Mansoura University, Egypt.

■ REFERENCES

- (1) Nur Mohammad, E. U.; Uddin, S.; Babar, I. H.; Hossain, S.; Bitu, N. A.; Khan, M. N.; Asraf, A.; Hossen, F.; Kudrat-E-Zahan, Md. Exploring Schiff Base Chemistry—An Overview. *Int. J. Chem. Pharm. Sci.* **2021**, *9*, 18–31.
- (2) Nassar, M. Y.; Ahmed, I. S.; Dessouki, H. A.; Ali, S. S. Synthesis and Characterization of Some Schiff Base Complexes Derived from 2,5-Dihydroxyacetophenone with Transition Metal Ions and Their Biological Activity. *J. Basic Environ. Sci.* **2018**, *5*, 60–71.
- (3) Silva, Y. F.; Riga, B. A.; Deflon, V. M.; Souza, J. R.; Silva, L. H. F.; Machado, A. E. H.; Maia, P. I. S.; Valdemiro P, C.-J.; Goi, B. E. Organometallic-Mediated Radical Polymerization Using Well-Defined Schiff Base Cobalt (II) Complexes. *J. Coord. Chem.* **2018**, *71*, 3776–3789.
- (4) Abubakar, M. J.; Husaini, M.; Nuhu, A. H. Synthesis and Characterization of Schiff Base of 3-[(2-Hydroxy-Phenylimino)-Methyl]-6-Methoxy-Quinolin-2-Ol and Its Metal Complexes and Their Evaluation for Antibacterial and Antifungal Activity. *Alger. J. Eng. Technol.* **2020**, *2*, 29–36.
- (5) Dalia, S. A.; Afsan, F.; Hossain, M. S.; Khan, M. N.; Zakaria, C.; Zahan, M. K. E.; Ali, M. A Short Review on Chemistry of Schiff Base Metal Complexes and Their Catalytic Application. *Int. J. Chem. Stud.* **2018**, *6*, 2859–2866.
- (6) Bekheit, M. M.; El-Shobaky, A. R.; Gad Allah, M. T. Synthesis, Spectroscopic Characterization and Antimicrobial Studies of Some Metal Complexes with 2-Acetylpyridine Phenoxyacetyl Hydrazone (HAPPA). *Arab. J. Chem.* **2017**, *10*, S3064–S3072.
- (7) Hall, I. H.; Peaty, N. J.; Henry, J. R.; Easmon, J.; Heinisch, G.; Pürstinger, G. Investigations on the Mechanism of Action of the Novel Antitumor Agents 2-Benzothiazolyl, 2-Benzoxazolyl, and 2-Benzimidazolyl Hydrazones Derived from 2-Acetylpyridine. *Arch. Pharm.* **1999**, *332*, 115–123.
- (8) Al Zoubi, W.; Al-Hamdani, A. A. S.; Ahmed, S. D.; Ko, Y. G. A New Azo-Schiff Base: Synthesis, Characterization, Biological Activity and Theoretical Studies of Its Complexes. *Appl. Organomet. Chem.* **2018**, *32*, No. e3895.
- (9) Bansod, A.; Bhaskar, R.; Ladole, C.; Salunkhe, N.; Thakare, K.; Aswar, A. Mononuclear Pyrazine-2-Carbohydrazone Metal Complexes: Synthesis, Structural Assessment, Thermal, Biological, and Electrical Conductivity Studies. *Eur. J. Chem.* **2022**, *13*, 126–134.
- (10) Filipović, N.; Todorović, T.; Marković, R.; Marinković, A.; Tufegđić, S. T.; Godevac, D.; Anđelković, K. Synthesis, Characterization and Biological Activities of N-Heteroaromatic Hydrazones and Their Complexes with Pd(II), Pt(II) and Cd(II). *Transit. Met. Chem.* **2010**, *35*, 765–772.
- (11) Abd El-Hady, M. N.; Zaky, R. R.; Ibrahim, K. M.; Gomaa, E. A. (E)-3-(2-(Furan-Ylmethylene)Hydrazinyl)-3-Oxo-N-(Thiazol-2yl)-Propanamide Complexes: Synthesis, Characterization and Antimicrobial Studies. *J. Mol. Struct.* **2012**, *1016*, 169–180.
- (12) Zaky, R. R.; Yousef, T. A. Spectral, Magnetic, Thermal, Molecular Modelling, ESR Studies and Antimicrobial Activity of (E)-3-(2-(2-Hydroxybenzylidene) Hydrazinyl)-3-Oxo- n(Thiazole-2-Yl)-Propanamide Complexes. *J. Mol. Struct.* **2011**, *1002*, 76–85.

- Divalent Co, Ni and Cu Complexes of Water-Soluble, Bioactive and Photoactive Thiosemicarbazone Salt. *J. Mol. Liq.* **2019**, *287*, 110958.
- (47) El-Metwally, N. M.; El-Shazly, R. M.; Gabr, I. M.; El-Asmy, A. A. Physical and Spectroscopic Studies on Novel Vanadyl Complexes of Some Substituted Thiosemicarbazides. *Spectrochim. Acta, Part A* **2005**, *61*, 1113–1119.
- (48) McGarvey, B. R. The Isotropic Hyperfine Interaction. *J. Phys. Chem.* **1967**, *71*, 51–66.
- (49) Onay, H.; Yerli, Y.; Öztürk, R. Synthesis and EPR Studies of Vanadyl Tetrakis(Selenodiazole)Porphyrzine. *Transit. Met. Chem.* **2009**, *34*, 163–166.
- (50) Karabulut, B.; ilkin, I.; Tapramaz, R. EPR and Optical Absorption Studies of VO₂+Doped Trisodium Citrate Dihydrate Single Crystals. *Z. Naturforsch., A: Phys. Sci.* **2005**, *60*, 95–100.
- (51) Kalkhoran, S.; Benowitz, N. L.; Rigotti, N. A. Reprint of: Prevention and Treatment of Tobacco Use. *J. Am. Coll. Cardiol.* **2018**, *72*, 2964–2979.
- (52) Li, L.; Zhang, F.; Zaia, J.; Linhardt, R. J. Top-down Approach for the Direct Characterization of Low Molecular Weight Heparins Using LC-FT-MS. *Anal. Chem.* **2012**, *84*, 8822–8829.
- (53) Mazzarino, M.; De La Torre, X.; Botrè, F.; Gray, N.; Cowan, D. A Rapid Screening LC-MS/MS Method Based on Conventional HPLC Pumps for the Analysis of Lowmolecular Weight Xenobiotics: Application to Doping Control Analysis. *Drug Test. Anal.* **2010**, *2*, 311–322.
- (54) Fetoh, A.; Mohammed, M. A.; Youssef, M. M.; Abu El-Reash, G. M. Characterization, Cyclic Voltammetry and Biological Studies of Divalent Co, Ni and Cu Complexes of Water-Soluble, Bioactive and Photoactive Thiosemicarbazone Salt. *J. Mol. Liq.* **2019**, *287*, 110958.
- (55) Fetoh, A.; Mohammed, M. A.; Youssef, M. M.; Abu El-Reash, G. M. Synthesis, Characterization, Cyclic Voltammetry and Biological Studies of Zn (II), Cd (II), Hg (II) and UO₂²⁺ Complexes of Thiosemicarbazone Salt. *Appl. Organomet. Chem.* **2019**, *33*, No. e4787.
- (56) Coats, A. W.; Redfern, J. P. Kinetic Parameters from Thermogravimetric Data. *Nature* **1964**, *201*, 68–69.
- (57) Horowitz, H. H.; Metzger, G. A New Analysis of Thermogravimetric Traces. *Anal. Chem.* **1963**, *35*, 1464–1468.
- (58) Hatakeyama, T.; Quinn, F. X. *Thermal Analysis: Fundamentals and Applications to Polymer Science*; Wiley, 1999.
- (59) Frost, A. A.; Pearson, R. G. *Kinetics and Mechanism*; John Wiley and Sons. Inc.: New York, 1961; p 19.
- (60) Kandil, S. S.; El-Hefnawy, G. B.; Baker, E. A. Thermal and Spectral Studies of 5-(Phenylazo)-2-Thiohydantoin and 5-(2-Hydroxyphenylazo)-2-Thiohydantoin Complexes of Cobalt (II), Nickel (II) and Copper (II). *Thermochim. Acta* **2004**, *414*, 105–113.
- (61) Maravalli, P. B.; Goudar, T. R. Thermal and Spectral Studies of 3-N-Methyl-Morpholino-4-Amino-5-Mercapto-1, 2, 4-Triazole and 3-N-Methyl-Piperidino-4-Amino-5-Mercapto-1, 2, 4-Triazole Complexes of Cobalt (II), Nickel (II) and Copper (II). *Thermochim. Acta* **1999**, *325*, 35–41.
- (62) Yusuff, K. K. M.; Sreekala, R. Thermal and Spectral Studies of 1-Benzyl-2-Phenylbenzimidazole Complexes of Cobalt (II). *Thermochim. Acta* **1990**, *159*, 357–368.
- (63) Huang, H.; Leung, D. Y. C.; Ye, D. Effect of Reduction Treatment on Structural Properties of TiO₂ Supported Pt Nanoparticles and Their Catalytic Activity for Formaldehyde Oxidation. *J. Mater. Chem.* **2011**, *21*, 9647–9652.
- (64) Fetoh, A.; Mohammed, M. A.; Youssef, M. M.; El-Reash, G. M. A. Investigation (IR, UV-visible, fluorescence, X-ray diffraction and thermogravimetric) studies of Mn(II), Fe(III) and Cr(III) complexes of thiosemicarbazone derived from 4-pyridyl thiosemicarbazide and monosodium 5-sulfonatosalicylaldehyde and evaluation of their biological applications. *J. Mol. Struct.* **2023**, *1271*, 134139.
- (65) Ma, S.; Zhang, J.; Liu, Y.; Qian, J.; Xu, B.; Tian, W. Direct Observation of the Symmetrical and Asymmetrical Protonation States in Molecular Crystals. *J. Phys. Chem. Lett.* **2017**, *8*, 3068–3072.
- (66) Wu, Z. Y.; Li, Y. T.; Xu, D. J. Diaqua(2,2'-Diamino-4,4'-Bi-1,3-Thiazole)Oxosulfatovanadium(IV) Tetrahydrate. *Acta Crystallogr., Sect. C: Cryst. Struct. Commun.* **2005**, *61*, 463–465.
- (67) Puttreddy, R.; Von Essen, C.; Peuronen, A.; Lahtinen, M.; Rissanen, K. Halogen Bonds in 2,5-Dihaloypyridine-Copper(II) Chloride Complexes. *CrystEngComm* **2018**, *20*, 1954–1959.
- (68) Kukovec, B. M.; Popović, Z.; Pavlović, G. A One-Dimensional CdII Coordination Polymer: Catena-Poly[Cadmium(II)-Bis-(μ-6-Methyl-Picolinato)]. *Acta Crystallogr., Sect. C: Cryst. Struct. Commun.* **2007**, *63*, 389–391.
- (69) Rezaee, R.; Montazer, M.; Mianehro, A.; Mahmoudirad, M. Single-Step Synthesis and Characterization of Zr-MOF onto Wool Fabric: Preparation of Antibacterial Wound Dressing with High Absorption Capacity. *Fibers Polym.* **2022**, *23*, 404–412.
- (70) Tamer, Ö.; Avci, D.; Dege, N.; Atalay, Y. S. Synthesis, crystal structure, photophysical properties, density functional theory calculations and molecular docking studies on Cd(II) complex of 4,4'-dimethyl-2,2'-dipyridyl. *J. Mol. Struct.* **2020**, *1202*, 127288.
- (71) Al-Fahemi, J. H.; Abdallah, M.; Gad, E. A. M.; Jahdaly, B. A. A. L. Experimental and Theoretical Approach Studies for Melatonin Drug as Safely Corrosion Inhibitors for Carbon Steel Using DFT. *J. Mol. Liq.* **2016**, *222*, 1157–1163.
- (72) Frisch, M.; Trucks, G. W.; Schlegel, H. B.; Scuseria, G. E.; Robb, M. A.; Cheeseman, J. R.; Scalmani, G.; Barone, V.; Mennucci, B.; Petersson, G.; et al. *Gaussian 09*, Revision D. 01; Gaussian, Inc.: Wallingford CT, 2009.
- (73) Addison, A. W.; Rao, T. N.; Reedijk, J.; van Rijn, J.; Verschoor, G. C. Synthesis, structure, and spectroscopic properties of copper(II) compounds containing nitrogen-sulphur donor ligands; the crystal and molecular structure of aqua[1,7-bis(N-methylbenzimidazol-2'-yl)-2,6-dithiaheptane]copper(II) perchlorate. *J. Chem. Soc., Dalton Trans.* **1984**, 1349–1356.
- (74) Fedorova, O. A.; Shepel, N. E.; Tokarev, S. D.; Lukovskaya, E. V.; Sotnikova, Y. A.; Moiseeva, A. A.; D'Aléo, A.; Fages, F.; Maurel, F.; Fedorov, Y. V. Intramolecular Electron Transfer in Cu(II) Complexes with Aryl-Imidazo-1,10-Phenanthroline Derivatives: Experimental and Quantum Chemical Calculation Studies. *New J. Chem.* **2019**, *43*, 2817–2827.
- (75) Altürk, S.; Avci, D.; Başoğlu, A.; Tamer, Ö.; Atalay, Y.; Dege, N. Copper(II) Complex with 6-Methylpyridine-2-Carboxylic Acid: Experimental and Computational Study on the XRD, FT-IR and UV-Vis Spectra, Refractive Index, Band Gap and NLO Parameters. *Spectrochim. Acta, Part A* **2018**, *190*, 220–230.
- (76) Ayisha Begam, K.; Kanagathara, N.; Marchewka, M. K.; Lo, A. Y. DFT, Hirshfeld and Molecular Docking Studies of a Hybrid Compound - 2,4-Diamino-6-Methyl-1,3,5-Triazin-1-Ium Hydrogen Oxalate as a Promising Anti-Breast Cancer Agent. *Heliyon* **2022**, *8*, No. e10355.
- (77) Chaudhary, M. K.; Srivastava, A.; Singh, K. K.; Tandon, P.; Joshi, B. D. Computational Evaluation on Molecular Stability, Reactivity, and Drug Potential of Frovatriptan from DFT and Molecular Docking Approach. *Comput. Theor. Chem.* **2020**, *1191*, 113031.
- (78) Toubi, Y.; Abridach, F.; Radi, S.; Souna, F.; Hakkou, A.; Alsayari, A.; Bin Muhsinah, A.; Mabkhot, Y. N. Synthesis, Antimicrobial Screening, Homology Modeling, and Molecular Docking Studies of a New Series of Schiff Base Derivatives as Prospective Fungal Inhibitor Candidates. *Molecules* **2019**, *24*, 3250.
- (79) Bayoumy, A. M.; Ibrahim, M.; Omar, A. Mapping Molecular Electrostatic Potential (MESP) for Fulleropyrrolidine and Its Derivatives. *Opt. Quant. Electron.* **2020**, *52*, 346–413.
- (80) El-Shereafy, S. E.; Gomaa, E. A.; Yousif, A. M.; Abou El-Yazed, A. S. Electrochemical and Thermodynamic Estimations of the Interaction Parameters for Bulk and Nano-Silver Nitrate (NSN) with Cefdinir Drug Using a Glassy Carbon Electrode. *Iran J. Mater. Sci. Eng.* **2017**, *14*, 48–57.
- (81) Hoogerheide, J. G.; Popov, A. I. Study of Monensin Complexes with Monovalent Metal Ions in Anhydrous Methanol Solutions. *J. Solution Chem.* **1978**, *7*, 357–372.

- (82) Gomaa, E. A.; Morsi, M. A.; Negm, A. E.; Sherif, Y. A. Cyclic Voltammetry of Bulk and Nano Manganese Sulfate with Doxorubicin Using Glassy Carbon Electrode. *Int. J. Nano Dimens.* **2017**, *8*, 89–96.
- (83) Chen, Z.; Bertin, R.; Frolidi, G. EC50 Estimation of Antioxidant Activity in DPPH* Assay Using Several Statistical Programs. *Food Chem.* **2013**, *138*, 414–420.
- (84) Abdelghany, A. M.; Menazea, A. A.; Ismail, A. M. Synthesis, Characterization and Antimicrobial Activity of Chitosan/Polyvinyl Alcohol Blend Doped with Hibiscus Sabdariffa L. Extract. *J. Mol. Struct.* **2019**, *1197*, 603–609.
- (85) Elimam, D. M.; Elgazar, A. A.; El-Senduny, F. F.; El-Domany, R. A.; Badria, F. A.; Eldehna, W. M. Natural Inspired Piperine-Based Ureas and Amides as Novel Antitumor Agents towards Breast Cancer. *J. Enzyme Inhib. Med. Chem.* **2022**, *37*, 39–50.
- (86) El-Senduny, F. F.; Shabana, S. M.; Rosel, D.; Brabek, J.; Althagafi, I.; Angeloni, G.; Manolikakes, G.; Shaaban, S. Urea-Functionalized Organoselenium Compounds as Promising Anti-HepG2 and Apoptosis-Inducing Agents. *Future Med. Chem.* **2021**, *13*, 1655–1677.
- (87) Abdellatif, K. R. A.; Belal, A.; El-Saadi, M. T.; Amin, N. H.; Said, E. G.; Hemeda, L. R. Design, Synthesis, Molecular Docking and Antiproliferative Activity of Some Novel Benzothiazole Derivatives Targeting EGFR/HER2 and TS. *Bioorg. Chem.* **2020**, *101*, 103976.
- (88) Kareem, F. A. K.; Al-Hujaj, H. H.; Jassem, A. M.; Al-Masoudi, N. A. A Click Synthesis, Molecular Docking, Cytotoxicity on Breast Cancer (MDA-MB 231) and Anti-HIV Activities of New 1,4-Disubstituted-1,2,3-Triazole Thymine Derivatives. *Russ. J. Bioorg. Chem.* **2020**, *46*, 360–370.
- (89) Chang, E. C.; Frasor, J.; Komm, B.; Katzenellenbogen, B. S. Impact of Estrogen Receptor β on Gene Networks Regulated by Estrogen Receptor α in Breast Cancer Cells. *Endocrinology* **2006**, *147*, 4831–4842.
- (90) Dhumad, A. M.; Jassem, A. M.; Alharis, R. A.; Almashal, F. A. Design, Cytotoxic Effects on Breast Cancer Cell Line (MDA-MB 231), and Molecular Docking of Some Maleimide-Benzenesulfonamide Derivatives. *J. Indian Chem. Soc.* **2021**, *98*, 100055.
- (91) Trott, O.; Olson, A. J. AutoDock Vina: Improving the Speed and Accuracy of Docking with a New Scoring Function, Efficient Optimization, and Multithreading. *J. Comput. Chem.* **2010**, *31*, 455–461.
- (92) Carcelli, M.; Mazza, P.; Pelizzi, C.; Zani, F. Antimicrobial and Genotoxic Activity of 2,6-Diacetylpyridine Bis(Acylhydrazones) and Their Complexes with Some First Transition Series Metal Ions. X-Ray Crystal Structure of a Dinuclear Copper(II) Complex. *J. Inorg. Biochem.* **1995**, *57*, 43–62.
- (93) Farhadi, F.; Khameneh, B.; Iranshahi, M.; Iranshahi, M. Antibacterial Activity of Flavonoids and Their Structure–Activity Relationship: An Update Review. *Phyther. Res.* **2019**, *33*, 13–40.
- (94) Aljahdali, M.; El-Sherif, A. A. Synthesis, Characterization, Molecular Modeling and Biological Activity of Mixed Ligand Complexes of Cu (II), Ni (II) and Co (II) Based on 1, 10-Phenanthroline and Novel Thiosemicarbazone. *Inorg. Chim. Acta.* **2013**, *407*, 58–68.
- (95) Gacche, R. N.; Jadhav, S. G. Antioxidant Activities and Cytotoxicity of Selected Coumarin Derivatives: Preliminary Results of a Structure-Activity Relationship Study Using Computational Tools. *J. Exp. Clin. Med.* **2012**, *4*, 165–169.
- (96) Parrilha, G. L.; Da Silva, J. G.; Gouveia, L. F.; Gasparoto, A. K.; Dias, R. P.; Rocha, W. R.; Santos, D. A.; Speziali, N. L.; Beraldo, H. Pyridine-Derived Thiosemicarbazones and Their Tin(IV) Complexes with Antifungal Activity against Candida Spp. *Eur. J. Med. Chem.* **2011**, *46*, 1473–1482.
- (97) Heidarpoor Saremi, L.; Ebrahimi, A.; Lagzian, M. Identification of New Potential Cyclooxygenase-2 Inhibitors: Insight from High Throughput Virtual Screening of 18 Million Compounds Combined with Molecular Dynamic Simulation and Quantum Mechanics. *J. Biomol. Struct. Dyn.* **2021**, *39*, 1717–1734.
- (98) Zaky, R.; Fekri, A. Solid State Ball Milling as a Green Approach to Prepare Cu(II) Complexes: Structural, Spectral, DFT, and DNA Studies. *New J. Chem.* **2017**, *41*, 4555–4563.
- (99) Fekri, A.; Zaky, R. Solvent-Free Synthesis and Computational Studies of Transition Metal Complexes of the Aceto- and Thioaceto-Acetanilide Derivatives. *J. Organomet. Chem.* **2016**, *818*, 15–27.